



Direct numerical simulation of turbulent elliptical pipe flow under system rotation about the major axis

Rafael Hurtado Rosas , Zhao-Ping Zhang, and Bing-Chen Wang *

*Department of Mechanical & Manufacturing Engineering, University of Manitoba,
Winnipeg, Manitoba R3T 5V6, Canada*



(Received 21 February 2021; accepted 29 July 2021; published 25 August 2021)

The effect of Coriolis forces on the turbulent flow in an elliptical pipe subjected to spanwise rotation about the major axis has been studied using direct numerical simulations (DNS). In response to the system rotation, large-scale secondary flows appear in the cross-stream plane as a pair of counterrotating vortices, which significantly impact the turbulence statistics and structures of the flow. To capture the most energetic turbulent eddy motions in the streamwise direction, the pipe length has been extended to $L_z = 20\pi b$ (here, b is the minor semiaxis of the elliptical pipe), which is the longest in the current literature for the study of elliptical pipe flows. Laminarization occurs on the suction side of the flow and propagates toward the pressure side as the speed of the system rotation increases. The system rotation imposed radically alters the budget balance of Reynolds stresses through its effects on the mean and turbulent flow fields and through the Coriolis term. At a moderate rotation number, the Coriolis term starts to dominate the energy transfer from $\langle w'w' \rangle$ to $\langle v'v' \rangle$, and also acts on $\langle v'w' \rangle$ as an additional source term. This mechanism far surpasses the role of the pressure-strain term, which undergoes a significant reduction in response to the system rotation. The characteristics of the turbulence field is investigated in both physical and spectral spaces through analyses of the first- and second-order statistical moments, as well as the budget balance of the Reynolds stress transport equation and coherent flow structures.

DOI: [10.1103/PhysRevFluids.6.084609](https://doi.org/10.1103/PhysRevFluids.6.084609)

I. INTRODUCTION

Turbulent flows confined within an elliptical pipe subjected to spanwise system rotation represent an interesting physical problem with engineering applications to centrifuges and rotary machinery. The Coriolis forces arising from the spanwise system rotation significantly affect the flow physics by inducing large-scale secondary flows. As such, it is important to investigate the effects of the Coriolis forces on the coherent structures and statistics of the turbulent elliptical pipe flows.

A. Rotating plane-channel flows

The topic of turbulent plane-channel flow subjected to spanwise system rotation has been studied extensively, through both experimental [1,2] and numerical [3–8] approaches. In their experimental study, Johnston *et al.* [1] observed the onset of laminarization on the suction side of the channel in response to spanwise system rotation, as well as an increase in the turbulence intensity on the pressure side of the channel. They also observed the formation of “roll-cells” on the pressure side of the channel in response to system rotation, and recognized these as a consequence of Taylor-Görtler

*BingChen.Wang@Umanitoba.ca

(TG) instability, similar to those arising in a flow over a wall with streamwise curvature. These observations were confirmed by Kristoffersen and Anderson [3] in their DNS study of rotating channel flow with a Reynolds number of $Re_b = U_b h / \nu \approx 2900$ and varying rotation numbers in the range of $0 \leq Ro_b = 2\Omega h / U_b \leq 0.5$ (where U_b is the bulk mean velocity, h is the half channel height, and Ω is the angular speed of system rotation around the spanwise axis). They observed that TG-like structures work to shift low-speed flow from the near-wall region toward the core turbulent region. Furthermore, they were able to examine the rotating effects on the Reynolds stresses. Grundestam *et al.* [5] performed a DNS study of spanwise rotating plane-channel flow at $Re_\tau = u_\tau h / \nu = 180$ (where u_τ is the wall friction velocity) for a greater range of rotation numbers of $0 \leq Ro_b \leq 3.0$, and observed complete flow laminarization at $Ro_b = 3.0$. Reductions of large-scale turbulence structures and local Reynolds number value Re_τ on the suction side of the channel were observed as the rotation number increased. The effects of system rotation on the budget balance of the Reynolds stresses was also studied, and it was determined that the Coriolis term serves to redistribute turbulence energy among different components of the Reynolds stress tensor. Wallin *et al.* [6] performed linear stability analysis along with DNS at $Re_\tau = 105, 130$, and 180 to study the laminarization mechanisms of the spanwise-rotating plane-channel flows. They discovered that at supercritical rotation numbers, the flow becomes dominated by a cycle of growing Tollmien-Schlichting (TS) waves, which break down into bursts of turbulence, and then the cycle repeats. Xia *et al.* [7] conducted a DNS study of the effects of spanwise rotation on the first- and second-order turbulence statistics of a plane-channel flow at $Re_\tau = u_\tau h / \nu = 180$ and rotation numbers in the range of $0 \leq Ro_\tau \leq 130$. They observed regions of linear behavior in the profiles of the root-mean-square (RMS) values of velocity fluctuations and Reynolds shear stresses. Brethouwer [8] performed DNS of spanwise rotating plane-channel flow with the Reynolds number varying from $Re_b = 3,000$ to 31,600 and the rotation number Ro_b varying from 0 to 2.7. The effects of the Coriolis forces were found to be strongly dependent on the Reynolds number, as flows of higher Reynolds numbers required higher rotation numbers to reach full laminarization. He confirmed the appearance of cyclical turbulence bursts in laminarized flow, previously observed by Wallin *et al.* [6].

Studies of streamwise-rotating channel flow have also been conducted extensively in the literature. Oberlack *et al.* [9] performed a group analysis of the main characteristics of the flow in a streamwise-rotating channel and verified their analytical predictions with DNS results at $Re_\tau = 180$. Recktenwald *et al.* [10] conducted both DNS and particle-image velocimetry (PIV) measurements of a streamwise rotating flow at $Re_\tau = 180$. Yang and Wang [11] performed DNS of streamwise-rotating plane-channel flow and determined that owing to the occurrence of very long TG-like vortices in the streamwise direction, extremely long computational domain lengths (up to $512\pi h$) were required to capture the most energetic eddies. Wu and Kasagi [12] analyzed the turbulent heat transfer within turbulent channel flows under arbitrary directional system rotation (at $Re_b = 4560$), and observed that the effects of spanwise rotation dominated the flow characteristics over those of streamwise and wall-normal rotations at comparable angular speeds of system rotation.

B. Rotating duct or pipe flows

In addition to the rotating plane-channel flows reviewed above, there have been experimental and numerical investigations into turbulent flows in rectangular ducts or circular pipes subjected to spanwise system rotation. In his pioneering work, Speziale [13] carried out a numerical study of spanwise-rotating laminar flow within a rectangular duct, and observed the emergence of a pair of counterrotating vortices in the cross-stream plane induced by the Coriolis forces. The streamwise velocity profiles were found to be adversely affected by the Coriolis forces, even causing the appearance of a small Taylor-Proudman (TP) region, which features zero mean streamwise velocity gradient along the axis of rotation. Pallares and Davidson [14] carried out large-eddy simulations (LES) of turbulent flow in a rotating square duct at $Re_\tau = 150$ (based on the mean wall friction velocity and half duct-height h) and rotation numbers in the range $0 \leq Ro_\tau = \Omega D_h / u_\tau \leq 0.75$.

They observed that the cross-stream flow induced by the Coriolis force radically changes the vortical flow structures typically occurring near the corners of a nonrotating duct. Also, they observed the emergence of a small TP region at high rotation numbers. Dai *et al.* [15] performed DNS of turbulent flow in a rotating square duct at $Re_\tau = 150$ and for $0 \leq Ro_\tau \leq 20$, and studied the mean characteristics of the rotating flow, such as the quasi Ekman layers on the sidewalls and the emerging TP regions. Fang *et al.* [16] conducted DNS to study the effects of spanwise rotation on turbulent flow within a square duct at $Re_\tau = 150$. They observed four pairs of counterrotating secondary vortices in a nonrotating square duct, which collapsed to a single pair at sufficiently high rotation numbers, in consequence of the Coriolis force. Zhang and Wang [17] performed a DNS study of turbulent flow in a circular pipe under radial rotation. A significant initial increase in the turbulence kinetic energy (TKE) on the pressure side of the pipe was observed at the lowest rotation number, followed by a monotonic trend toward laminarization as the rotation number continues to increase.

C. Stationary elliptical pipe flows

In the literature, only a few studies of stationary (nonrotating) turbulent elliptical pipe flow are available. Cain and Duffy [18] conducted measurements using Pitot tubes to determine the wall friction coefficient of airflow in elliptical pipes of aspect ratios $AR = 1.5:1$ and $2:1$ at Reynolds numbers $Re_{D_h} = 2 \times 10^4 \sim 1.3 \times 10^5$. Here, the aspect ratio is defined as $AR = a : b$ where a and b semimajor and semiminor axes of the elliptical pipe. The Reynolds number is defined as $Re_{D_h} = U_b D_h / \nu$, where D_h is the hydraulic diameter. Cain and Duffy confirmed the existence of self-similar nondimensionalized mean velocity profiles near the wall and observed that the wall shear stress is sensitive to the azimuthal positions of the pipe. Nikitin and Yakhot [19] performed a DNS study of flows confined within stationary elliptical pipes of $AR = 2:1$ and $1.5:1$ at $Re_{D_h} = 6000$. They observed that the local wall friction velocity varies azimuthally, and the turbulence statistics along the minor axis were similar to those of a plane-channel flow. Voronova and Nikitin [20] further conducted DNS at $Re_{D_h} = 4000$ and $AR = 2:1$ and analyzed the mean velocity and basic turbulence characteristics of the flow. Later, Voronova and Nikitin [21] refined their DNS research of nonrotating elliptical pipe flows by increasing the Reynolds number to $Re_{D_h} = 6000$.

D. Objectives

Based on a thorough literature study, it is confirmed that, thus far, no study of rotating elliptical pipe flows has been reported in the literature. In view of this, the first objective of this research is to systematically investigate the effects of spanwise system rotation (about the major axis) on the flow and structures confined within an elliptical pipe using DNS. To this purpose, the statistical moments of the elliptical pipe flows under system rotation are compared against those of stationary elliptical pipe flows. In total, eight rotation numbers, ranging widely from $Ro_\tau = \Omega D_h / u_{\tau 0S} = 0$ to 24.0 are compared. The flow regime varies from being fully turbulent at low rotation numbers to being fully laminarized at the highest rotation number tested. The Coriolis effects on the first and second-order statistical moments, premultiplied energy spectra, budget balance of Reynolds stresses and coherent flow structures are thoroughly investigated.

Furthermore, it is observed that in the current literature, a systematic study of the minimum pipe length for precisely conducting DNS of both nonrotating and rotating elliptical pipe flows is still lacking. As the second objective of this research, we aim at using a very long pipe length of $L_z = 20\pi b$ to conduct the analysis of DNS data in both physical and spectral spaces. We will explain why such a long domain length is necessary to properly capture the streamwise length-scales of the most energetic eddy motions in both nonrotating and rotating elliptical pipe flows; and by contrast, why the elliptical pipe lengths used in the current literature of DNS of nonrotating elliptical pipe flows are mostly insufficient for accurately performing DNS. All the results presented in the paper are based on a fixed pipe length of $L_z = 20\pi b$ (which is the default pipe length), except that in the our comparative study of the pipe length effects using the two-point autocorrelation coefficient,

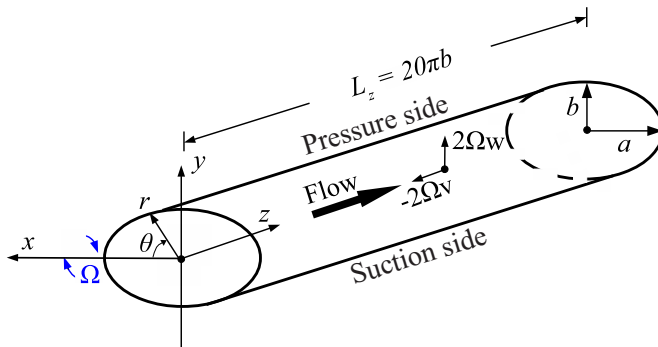


FIG. 1. Computational domain of a spanwise-rotating elliptical pipe in the Cartesian coordinate system. The major and minor semiaxes are denoted as a and b , respectively. The two Coriolis force components $2\Omega w$ and $-2\Omega v$ are shown in the y and z directions, respectively, resulting from the spanwise rotation about the major (x) axis.

four additional shorter pipe length cases are tested independently using DNS (with $L_z = 2\pi b$, $5\pi b$, $8\pi b$, and $12\pi b$) for two nonrotating and rotating flow cases (of rotation numbers $Ro = 0.0$ and 1.0). Thus, in total, 16 test cases are involved in this research. Besides the previously mentioned eight test cases of varying rotation numbers $Ro_\tau = 0.0$ - 24.0 (based on a fixed pipe length $L_z = 20\pi b$), there are also eight test cases of shorter pipe length cases (for the study of two-point autocorrelation coefficient only, at $Ro = 0.0$ and 1.0).

The remainder of this paper is organized as follows: In Sec. II, the test case and numerical algorithm for conducting DNS are introduced. In Sec. III, the first- and second-order statistics of the velocity field, as well as the spectra of velocity fluctuations, budget terms of Reynolds stresses transport equations, and turbulent flow structures are analyzed. Finally, in Sec. IV, major conclusions of this research are summarized.

II. TEST CASE AND NUMERICAL METHOD

DNS has been conducted for fully turbulent flow confined within an elliptical pipe of $AR = 2:1$ at a fixed nominal Reynolds number $Re_\tau = u_\tau D_h / 2\nu = 180$ (or, equivalently, $Re_{D_h} \approx 5300$) for a wide range of rotation numbers of $Ro_\tau = 0.0, 0.25, 0.5, 1.0, 4.0, 8.0, 16.0$, and 24.0 . Figure 1 shows the computational domain, coordinate system, and direction of the system rotation. In the figure, x , y and z represent the spanwise, wall-normal and streamwise coordinates, with the corresponding velocity components being u , v and w , respectively. In response to system rotation, two Coriolis force components $2\Omega w$ and $-2\Omega v$ appear in the y and z directions, respectively. In Fig. 1, the vertical (or y) component of the Coriolis force points toward the top side of the elliptical pipe, causing the pressure level of the fluid to enhance on this side. This side is therefore referred to as the pressure side. Correspondingly, the bottom side of elliptical pipe is referred to as the suction side, which features a reduced pressure caused by the same y component of the Coriolis force.

In the DNS study of nonrotating elliptical pipe flows conducted by Nikitin and Yakhot [19] and Voronova and Nikitin [20,21] the pipe lengths were kept at $L_z = 6D_h \approx 5\pi b$ (Nikitin and Yakhot) and $6a \approx 3.8\pi b$ (Voronova and Nikitin). The pipe length of $L_z = 20\pi b$ tested here is the longest in the current literature of nonrotating turbulent elliptical pipe flows. In Sec. III C, it will be explained why such a long domain length is necessary to properly capture the streamwise length scales of the most energetic eddy motions.

The flow is incompressible, governed by the continuity and momentum equations, expressed as

$$\frac{\partial u_i}{\partial x_i} = 0, \quad (1)$$

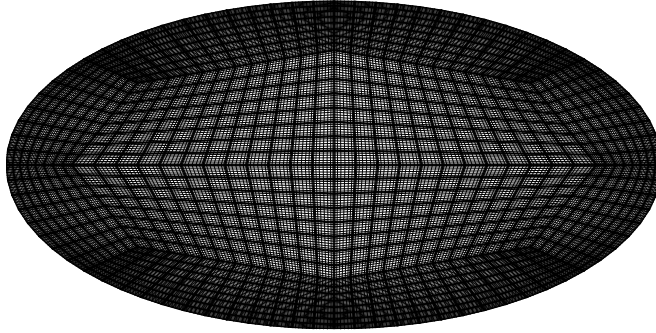


FIG. 2. Cross-sectional view of the mesh. The domain is discretized into 1024 quadrilateral elements using a spectral-element method. Each element is constructed using a eighth-order Gauss-Lobatto-Legendre-Lagrange polynomial. The mesh is then expanded in the streamwise direction through 960 modes (not shown).

and

$$\frac{\partial u_i}{\partial t} + u_j \frac{\partial u_i}{\partial x_j} = -\delta_{i3}\Pi - \frac{1}{\rho} \frac{\partial p}{\partial x_i} + \nu \frac{\partial^2 u_i}{\partial x_j^2} + 2\epsilon_{1ij}\Omega u_j, \quad (2)$$

respectively. Here, subscripts $i, j = 1, 2,$ and 3 denote the $x, y,$ and z directions, respectively; and $u_i, \rho, p,$ and ν represent the velocity, density, pressure, and kinematic viscosity of the fluid, respectively. As shown in Fig. 1, for the velocity field, both methods of tensor notation and components are used, whichever is convenient (with $u_1, u_2,$ and u_3 corresponding to u, v and $w,$ respectively). Symbol Ω denotes the constant angular rotating speed around the x axis, Π represents the constant mean pressure gradient in the z direction that is required to drive the flow, and δ_{ij} and ϵ_{ijk} are the Kronecker delta and Levi-Civita symbol, respectively.

The spectral-element code so-called ‘‘Semtex’’ developed by Blackburn and Sherwin [22] was used to solve the governing equations for the instantaneous $u, v, w,$ and p fields. It is written in the $C++$ and FORTRAN programming languages, and parallelized using message passing interface (MPI) libraries. This spectral-element in-house computer code is highly accurate for performing DNS of incompressible flows for transient problems on a UNIX/LINUX server [22,23]. Time integration is carried out through a three-step second-order time-splitting scheme. In the first temporal substep, an intermediate velocity is obtained by applying a second-order backward-time differencing scheme to the convection term and provided body-forces (Π and Coriolis forces). In the second temporal substep, this intermediate velocity is used to calculate the pressure field, based on a pressure-correction method applied to the flow field by enforcing the continuity requirement. In the third and final temporal substeps, the viscous terms of Eq. (2) are implicitly integrated with the provided boundary conditions. The equations of the second and third substeps are represented as two-dimensional Helmholtz equations, which are solved in the spectral space using a static condensation technique [23].

Figure 2 shows a cross-sectional view of the mesh used for DNS. It was generated through a MATLAB script. The central octagonal structure within the log-law region of the flow was first constructed for meshing the pipe center. Then, the outer grid structures were generated by progressively refining the internodal wall-normal distance as the wall is approached. The mesh is similar to those used by Di Liberto *et al.* [24] and Bolis *et al.* [25] in their simulations of nonrotating circular pipe flows. An eighth-order Gauss-Lobatto-Legendre-Lagrange nodal-based expansion was used for spatial discretization, in which the elliptical pipes were divided into 1024 quadrilateral elements. Along the axial direction, the mesh was expanded into 960 Fourier modes with $\Delta_z^+ = 9.08$ (measured in wall units calculated using $u_{\tau 0S}$, the time-, axially, and peripherally averaged wall-friction velocity of the stationary case). The wall-normal coordinate is $\Delta_n^+ = 0.21$ at

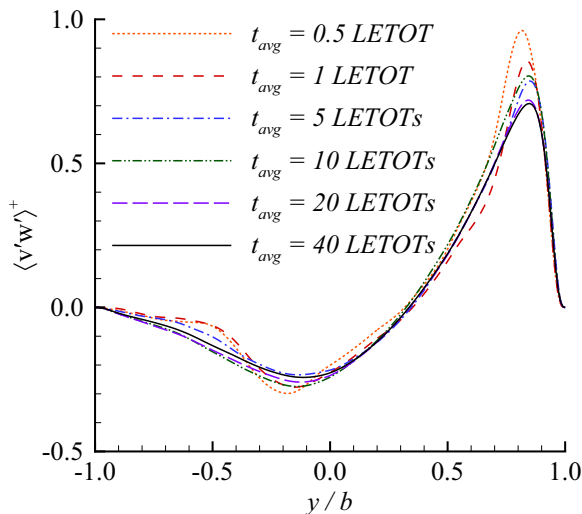


FIG. 3. Profiles of the Reynolds shear stress $\langle v'w' \rangle^+$ along the pipe minor axis (for $\theta = 90^\circ$ or 270°) at $Ro_\tau = 1.0$, averaged over different time durations (t_{avg}). The profiles have been nondimensionalized using $u_{\tau 0S}^2$.

the first node off the wall, and the resolution satisfies $0.61 < \Delta_n^+ < 3.36$ at the nodes near the pipe center. Here, Δ_n^+ represents the wall-normal spacing in wall units measured from the edge of each quadrilateral cell. The mean grid spacing, calculated as $\Delta^+ = (\Delta_x^+ \Delta_y^+ \Delta_z^+)^{1/3}$, has a maximum value of 4.03 (occurring in the elements near the pipe center). The grid resolution is kept sufficiently fine to satisfy the demanding requirement of DNS. Following Pope [26] and Eggels [27], the grid used in this study is able to resolve scales down to $\pi \eta^+$ (where η^+ is the calculated Kolmogorov scale in wall units), which varies in the range of $4.7 \leq \pi \eta^+ \leq 9.8$ throughout the entire computational domain. The current grid resolution (63.2 million grid points in total) is comparable to those used by Wu and Moin [28], Chin *et al.* [29], and Eggels *et al.* [27] in their DNS studies of turbulent flow in nonrotating circular pipes, and exceeds the grid resolution used in Nikitin and Yakhot [19] and Voronova and Nikitin [21], who performed DNS studies of nonrotating elliptical pipe flows.

To demonstrate the temporal convergence of the velocity statistics, the Reynolds shear stress $\langle v'w' \rangle^+$ has been computed using different time durations for $0.5 \leq t_{avg} \leq 40$ large-eddy turnover times (LETOTs, defined as $a/u_{\tau 0S}$). The results are presented in Fig. 3. From the figure, it is clear that temporal convergence improves as the averaging time t_{avg} increases, and an excellent agreement is observed between the profiles obtained using $t_{avg} = 20$ and 40 LETOTs. The results presented in the present study have been averaged over 40 LETOTs for rotating flow cases and over 80 LETOTs for the nonrotating flow case. The convergence performance of the rotating pipe flows is better than that of the nonrotating flow. This is because the flow field becomes dominated by the secondary flows in response to the appearance of the Coriolis forces in a rotating elliptical pipe flow (to be investigated in Sec. III). To further justify the selected time duration, we may consider the work of Nikitin and Yakhot (2005), who performed DNS of nonrotating circular and elliptical pipe flows at a similar Reynolds number. They used 5–10 LETOTs for circular pipe flows, and 50–110 LETOTs for elliptical pipe flows. It should be indicated that for the nonrotating test case ($Ro_\tau = 0.0$), the actual size of the sampling data at each time step is comparable to or even larger than that of Nikitin and Yakhot [19] due to the fact that the pipe length used in this study is four times that used in Nikitin and Yakhot [19]. Also, it would be beneficial to consider the classical work of Kim *et al.* [30], who used 10 LETOTs for calculating the velocity statistics of a plane-channel flow. For an elliptical pipe flow, the velocity field is homogeneous in the axial direction but inhomogeneous in the azimuthal

direction. Thus, the calculation of velocity statistics takes a much longer time for an elliptical pipe flow than for a turbulent plane-channel flow as in Kim *et al.* [30].

DNS was performed and data were stored on the WestGrid (Western Canada Research Grid) supercomputers. For each simulated case of rotating flows, 300 instantaneous flow fields (with data of approximately 7.0 TB) were generated. However, for the nonrotating flow case, the computational effort doubles.

In this paper, an instantaneous flow variable (such as u) is decomposed into a mean component and a fluctuating component, i.e., $u = \langle u \rangle + u'$. The mean component $\langle u \rangle$ is calculated based on averaging over time and over the homogeneous axial (z) direction. In a fully developed steady-state spanwise-rotating elliptical pipe flow (about the major axis), the flow is statistically stationary and is homogeneous in the axial direction. From Fig. 1, it is clear that the wall friction force is influenced by two axial forces (i.e., the axial pressure gradient and the axial component of the Coriolis force), and furthermore, the surface curvature varies along the periphery of the elliptical pipe. Therefore, the local time- and axially averaged mean friction velocity $u_\tau = \sqrt{\nu |\partial \langle w \rangle / \partial n|_{\text{wall}}}$ is a function of the mean axial pressure gradient Π , azimuthal position θ , and rotation number Ro_τ , i.e., $u_\tau = f(\Pi, \theta, \text{Ro}_\tau)$. Here, n denotes the normal direction of the elliptical pipe wall. This functional relationship is much more complex than that of the classical benchmark test case of a stationary plane-channel or circular pipe flow, in which the value of u_τ varies with Π only, i.e., $u_\tau = f(\Pi)$. Different from the rotating elliptical pipe flow case studied here, the condition is much simpler in the classical case of a stationary plane-channel or circular pipe flow, because the Coriolis force is absent and there exists spanwise/azimuthal homogeneity. Given the complexity of the flow described above, care must be taken in the nondimensionalization process associated with the wall coordinate in the current study. In presenting our results, superscript “+” denotes a variable that is nondimensionalized based on the kinematic viscosity ν of the fluid and the wall friction velocity. Three types of wall friction velocities are used in this research:

- (1) the time- and axially averaged local wall friction velocity, i.e., $u_\tau = f(\Pi, \theta, \text{Ro}_\tau)$;
- (2) the time- and axially averaged local wall friction velocity of the nonrotating elliptical pipe flow, i.e., $u_{\tau 0} = f(\Pi, \theta)$ (for $\text{Ro}_\tau \equiv 0$); and
- (3) the time- and surface-averaged wall friction velocity of the nonrotating elliptical pipe flow case, i.e., $u_{\tau 0S} = f(\Pi) = \oint_P u_{\tau 0} dl / C$ (for $\text{Ro}_\tau \equiv 0$), where P denotes periphery and C is the perimeter of an ellipse.

The need of these three types of wall friction velocities in the study of a rotating elliptical pipe flow (typically in the nondimensionalization process of a turbulence variable) is as follows. In the nondimensionalization process, use of u_τ facilitates the investigation of the local wall-scaling behavior of the flow at a specific rotation number (of a specific test case); use of $u_{\tau 0}$ facilitates the investigation of the trend of the local wall scaling behavior of the flow with a varying rotation number (in comparison with the nonrotating case); and in addition, use of $u_{\tau 0S}$ facilitates a general fair comparison of the statistic profiles of the whole flow field of different rotation numbers. The value of $u_{\tau 0S}$ varies with Π only and is independent of either Ro_τ or θ . Thus, when $u_{\tau 0S}$ is used in the nondimensionalization process, the rotating effects on the flow can be unambiguously demonstrated (with a reference to the nonrotating case), and the effect of peripheral surface curvature of the elliptical pipe is completely shielded off (through the peripheral averaging in its definition).

III. RESULTS

In this section, DNS results of spanwise-rotating elliptical pipe flows are analyzed and compared against those of the nonrotating flow. In total sixteen cases are considered, with the rotation number ranging from $\text{Ro}_\tau = 0$ to 24.0. The effects of Coriolis forces on the elliptical pipe flow are investigated in both physical and spectral spaces, including the analyses of the instantaneous and mean axial velocity fields, second-order turbulence statistics, budget balance of the Reynolds stress transport equation, premultiplied spectra of velocity fluctuations, and coherent structures.

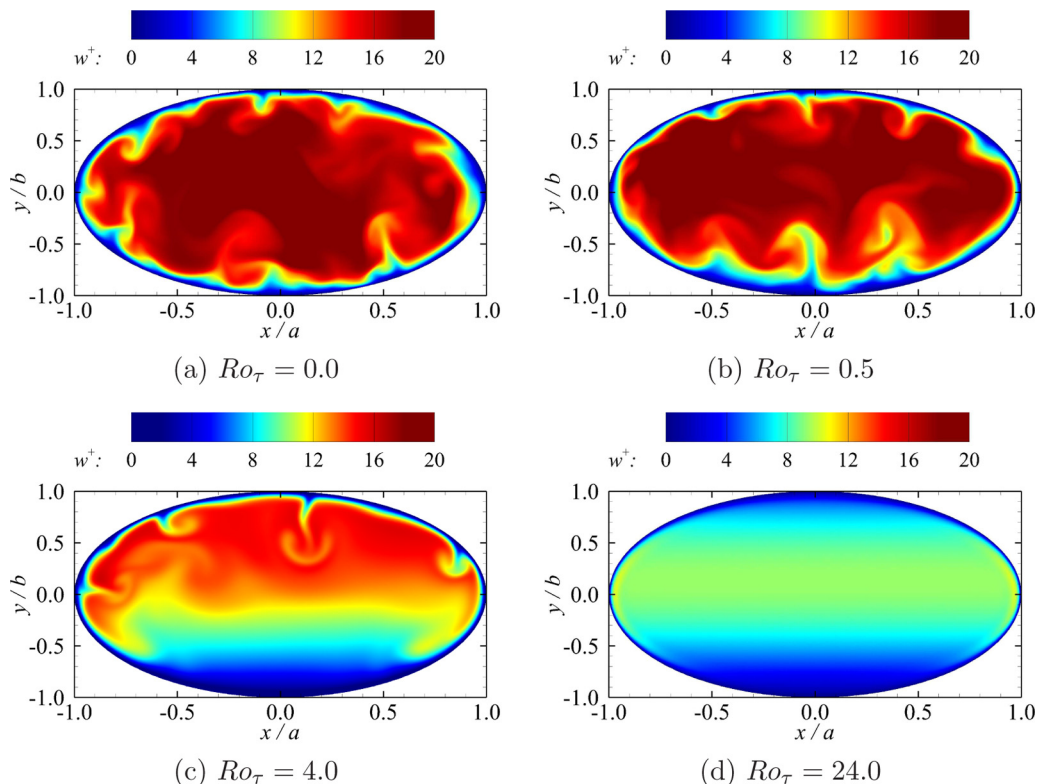


FIG. 4. Contours of the instantaneous axial velocity w^+ nondimensionalized using $u_{\tau 0S}$ at four different rotation numbers.

A. Instantaneous flow

Figure 4 compares the contour patterns of instantaneous axial velocity w^+ of four rotation numbers. Figure 4(a) shows that in the nonrotating case ($Ro_\tau = 0$), the central region of the pipe is dominated by high-momentum large-scale structures, while the near-wall regions are dominated by viscously retarded fluid motions. Along the periphery of the elliptical pipe, it is seen that the low-momentum fluid bursts into the center of the pipe in “mushroom patterns,” which are similar to those observed by Wu and Moin [28] in their DNS study of stationary circular pipe flow. As the rotation number increases to $Ro_\tau = 0.5$, the low-momentum area on the suction side of the pipe expands, as shown in Fig. 4(b). From Fig. 4(c), it is evident that as the rotation number further increases to $Ro_\tau = 4.0$, the spread of laminarization from the suction side of the pipe becomes apparent, as well as the formation of two high-momentum “legs” near the lower portion of the two sides. As the Coriolis forces push high-momentum fluid from the center of the pipe to its top side (or pressure side), the fluid travels downwards along the periphery of the pipe, resulting in the formation of the two aforementioned “legs” on the bottom side (or suction side) of the pipe. Furthermore, the location of the maximum velocity shifts toward the pressure side of the pipe and the magnitude of the axial velocity falls considerably throughout the entire pipe, especially on its suction side. The slowing down of the axial velocity is a result of the axial or z component of the Coriolis force $-2\Omega v$ induced by the spanwise system rotation (see Fig. 1), which points to the opposite direction of the mean flow. As is evident in Fig. 4(d), at the highest rotation number tested $Ro_\tau = 24.0$, complete laminarization is observed across the entirety of the pipe.

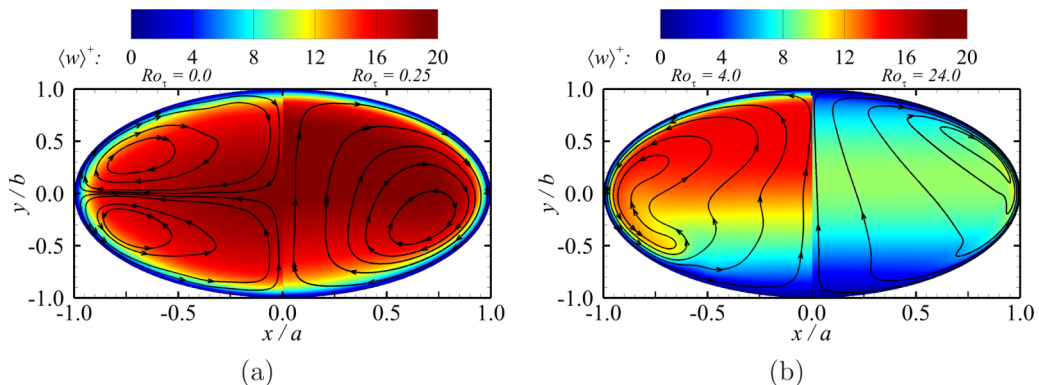


FIG. 5. Contours of the mean axial velocity $\langle w \rangle^+$ nondimensionalized using $u_{\tau 0S}$ with superimposed streamlines of the mean secondary flows in the cross-stream plane at $Ro_\tau = 0.0, 0.25, 4.0,$ and 24.0 . The averaging time is over 40 LETOTs for rotating flow cases and over 80 LETOTs for the nonrotating flow case.

B. Mean flow

Figure 5 compares the mean axial velocity fields (as well as the streamlines of the mean secondary flows in the cross-stream plane) of flows at $Ro_\tau = 0.0, 0.25, 4.0,$ and 24.0 . Because the mean flow field is symmetrical about the y axis, only half of the cross-section is shown for each rotation number. This method also facilitates a direct comparison of the mean flow patterns of different rotation numbers. For the turbulent flow confined within a stationary elliptical pipe (at $Ro_\tau = 0.0$) as shown in the left half of Fig. 5(a), the mean flow pattern is axial-symmetric, and large secondary flows appear in the nonrotating flow as two pairs of counterrotating vortical structures (with a mean flow vortex occupying each quadrant of the cross-section of the elliptical pipe). This mean flow pattern of the nonrotating elliptical pipe flow is consistent with the observations of Nikitin and Yakhot [19] and Voronova and Nikitin [21]. As soon as the system rotation is imposed, the mean flow pattern changes considerably under the influence of the Coriolis force (see Fig. 1). At $Ro_\tau = 0.25$ as shown in the right half of Fig. 5(a), the vertical component of the Coriolis force (i.e., $2\Omega(w)$) induces a mean secondary flow in the positive y direction, causing the two pairs of vortices (naturally occurring in the nonrotating elliptical pipe flow) to collapse into a single pair of counterrotating vortices, separated by the central vertical plane ($x/a = 0$). Clearly, the mean vortex center is located on the bottom suction side of the elliptical pipe at $Ro_\tau = 0.25$. From Fig. 5(b), it is seen that as the rotation number further increases to $Ro_\tau = 4.0$ and 24.0 , the cores of the mean flow vortical structures migrate toward the top side of the elliptical pipe. From Figs. 4(c), 4(d), and 5(b), it is evident that a Taylor-Proudman (TP) region exists at higher rotation numbers, which features $\partial\langle w \rangle/\partial x \approx 0$. The observation of a TP region in an elliptical pipe flow here is similar to that observed by Fang *et al.* [16] who conducted a DNS study of turbulent flows in a rotating square duct. From Fig. 5(b), it is clear that within the TP region, $\langle v \rangle$ is positively valued as a direct consequence of the vertical driving force (or, the mean Coriolis force component $2\Omega(w)$). The axial component of the mean Coriolis force is $-2\Omega\langle v \rangle$, which acts against the axial momentum of the flow. This “retarding” effect of the axial Coriolis force component is evidenced by Fig. 6(a), which shows that the bulk mean velocity of the pipe decreases monotonically with an increasing rotation number (for $Ro_\tau > 0.25$). At $Ro_\tau = 0.25$, however, a small (0.9%) increase is observed in the bulk mean velocity, which is similar to the observation of Zhang and Wang [17] in their DNS study of rotating circular pipe flows. At $Ro_\tau = 24.0$, the flow becomes fully laminarized in response to the strong Coriolis forces induced by the system rotation, and the bulk mean velocity is the smallest among all eight test cases of different rotation numbers (for a fixed pipe length of $L_z = 20\pi b$).

Figure 6(b) compares the time- and axially averaged wall friction velocities u_τ at different positions along the periphery of the elliptical pipe. In the figure, superscripts “ t ” and “ b ” denote the

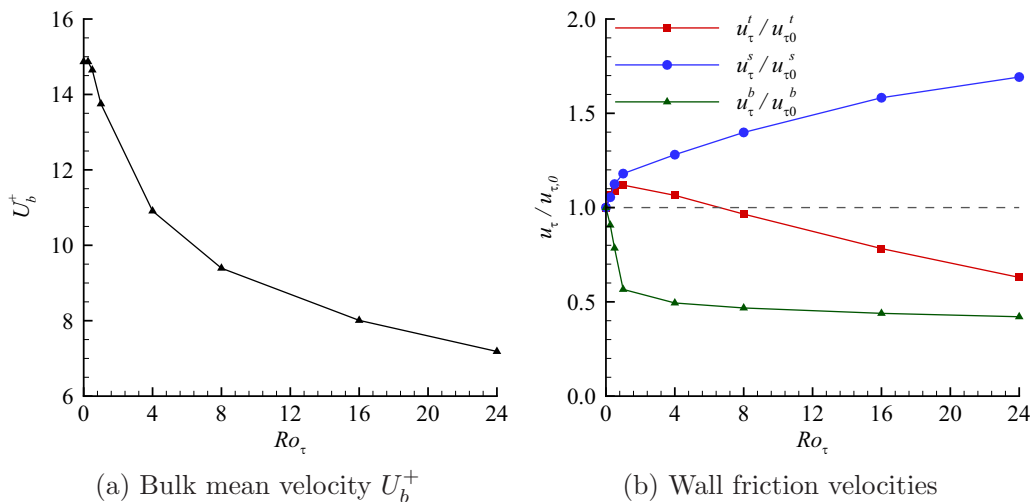


FIG. 6. Bulk mean velocity U_b^+ nondimensionalized using $u_{\tau 0S}$ and nondimensionalized wall friction velocities $u_\tau / u_{\tau 0}$ at different rotation numbers. Superscripts t , s , and b correspond to azimuthal locations $\theta = 90^\circ$, 180° (or 360°), and 270° , respectively.

end points at the top and bottom of the minor axis, respectively, while “ s ” denotes either end point of the major axis. To make a fair comparison of cases of different rotation numbers, the wall friction velocities have been nondimensionalized by $u_{\tau 0}$, which is the time- and axially averaged local wall friction velocity of the nonrotating elliptical pipe flow. As such, the value of the nondimensionalized wall friction velocity is unity at $Ro_\tau = 0$ in Fig. 6(b). As soon as the system rotation is imposed, the vertical component ($2\Omega\langle w \rangle$) of the Coriolis force pushes high momentum flow toward the top wall, which initially leads to an increase in the wall friction velocity on the pressure side of the pipe. Figure 6(b) shows that in response to the imposed system rotation, the value of $u_\tau^t / u_{\tau 0}^t$ initially increases by 12% in the range $0 \leq Ro_\tau \leq 1.0$, after which, it decreases monotonically due to the enhanced axial component ($-2\Omega\langle v \rangle$) of the Coriolis force which opposes the axial flow. On the bottom side of the wall, the induced secondary flow pushes viscously retarded fluid toward the pressure side of the pipe, thereby drastically reducing the axial velocity gradient on the suction side of the pipe. At a low rotation number $Ro_\tau = 0.25$, the wall friction velocity decreases by 9.4%. The wall friction velocity on the sides of the pipe ($u_\tau^s / u_{\tau 0}^s$) shows a monotonic increasing trend as the rotation number increases. The pair of counterrotating vortical structures in the cross-stream plane (shown in Fig. 5) transports high-momentum fluid from the center to the top side of the elliptical pipe, then the flow splits and further transports the fluid peripherally along the pipe wall to the two ends of the major axis, where an increase in the local wall-normal axial velocity gradient is observed. In addition to this, the value of $\langle v \rangle$ near the ends of the major axis is negative (see Fig. 5), resulting in a mean positive axial component of the Coriolis force ($-2\Omega\langle v \rangle$) in these regions, which accelerates the flow and leads to an even greater local wall-normal gradient of the mean axial velocity. These results are qualitatively similar to those obtained by Fang *et al.* [16] in their DNS study of rotating square duct flows.

The nondimensionalized mean axial velocity profiles at different rotation numbers along the minor and major axes are shown in Fig. 7. It is clear in Fig. 7(a) that the peak value of $\langle w \rangle^+$ decreases monotonically along the minor axis as the rotation number increases. Furthermore, as the rotation number increases from $Ro_\tau = 0.0$ to 1.0, the peak location moves toward the pressure side of the pipe. At higher rotation numbers, however, the peak location appears to move back toward the center of the pipe, as the Coriolis forces near the pressure side become more intense which further reduce the axial velocity near the pressure side of the pipe. Figure 7(b) shows that even at the lowest

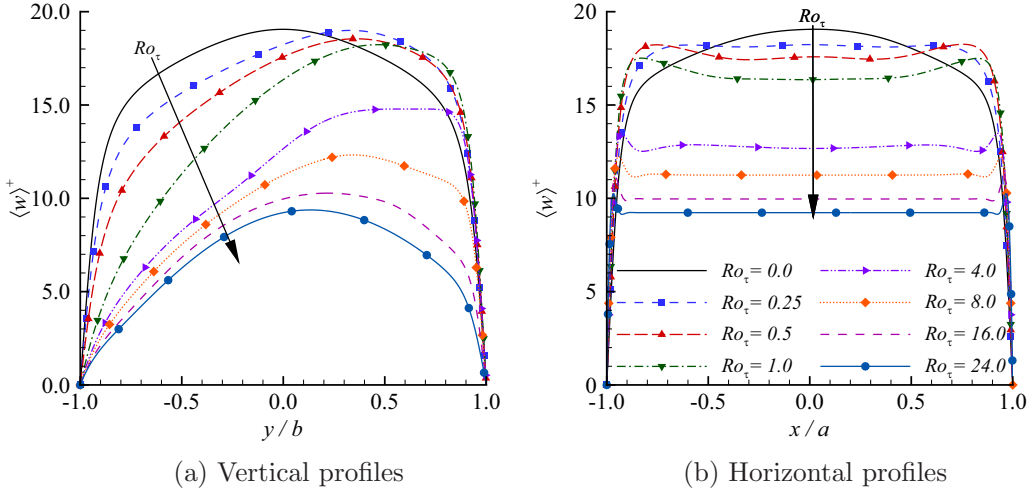


FIG. 7. Profiles of the mean axial velocity $\langle w \rangle^+$ in the vertical plane ($\theta = 90^\circ$ or 270°) and horizontal plane ($\theta = 0^\circ$ or 180°) at $Ro_\tau = 0.0, 0.25, 0.5, 1.0, 4.0, 8.0, 16.0$, and 24.0 . The profiles are nondimensionalized using $u_{\tau 0S}$. The arrow indicates a monotonic trend with an increasing Ro_τ .

rotation number ($Ro_\tau = 0.25$), a TP region appears along the major axis of the pipe, which features a flat profile along the axis of rotation (i.e., $\partial \langle w \rangle / \partial x \approx 0$). As the rotation number increases, the extent of this TP region grows. It is also interesting to point out that, along the major axis, the mean axial velocity peaks near the wall. This is because the Coriolis forces and the closed elliptical boundary jointly facilitate the development of cross-stream flow in the negative y direction in this region (such that the value of $\langle v \rangle$ is negative near the ends of the major axis, as shown previously in Fig. 5), which further leads to a positively valued Coriolis force ($-2\Omega \langle v \rangle$) in the axial direction. In consequence, the axial flow is accelerated locally to form the near-wall peaks of the mean axial velocity $\langle w \rangle^+$ close to the two ends of the major axis in Fig. 7(b). As the rotation number increases, these peaks become sharper in the near-wall region along the major axis, which is a reflection of an enhanced axial Coriolis force component.

Figure 8 shows the mean axial velocity profiles in wall coordinates, measured from both the suction and pressure sides of the pipe (correspondingly, the mean velocity $\langle w \rangle^+$ is nondimensionalized by u_τ^b and u_τ^+ , respectively). For the purpose of the comparison, the classical law-of-the-wall of von Kármán for a circular pipe flow is also displayed. For the purpose of comparison, the DNS data of Nikitin and Yakhot [19] for a nonrotating elliptical pipe flow ($Ro_\tau = 0$) are also presented, which show an excellent agreement with the current result in a wall coordinate system, a characteristic of inner similarity of a turbulent boundary layer. As is clear in both Figs. 8(a) and 8(b), the profile of the nonrotating case ($Ro_\tau = 0$) shows a good agreement with the familiar classical linear law of the wall (i.e., $\langle w \rangle^+ = y^+$) in the viscous sublayer, but the profile slightly overshoots the prediction of the classical log law (i.e., $\langle w \rangle^+ = 2.5 \ln y^+ + 5.5$) of von Kármán as a consequence of the significant transverse curvature of the elliptical pipe wall. Figure 8(a) shows that at $Ro_\tau = 0.25$, this discrepancy increases as a result of high-momentum fluid being transported toward the pressure side of the pipe by the secondary flow. As shown in Fig. 8(a), in the range $0.25 \leq Ro_\tau \leq 8.0$, as a result of the strengthening of the axial component of the Coriolis force ($-2\Omega \langle v \rangle$), a significant drop is observed in the magnitude of $\langle w \rangle^+$ in comparison with the classical log law of von Kármán. Interestingly, as the rotation number continues to increase in the range for $Ro_\tau \geq 8.0$, an increase in the value of $\langle w \rangle^+$ is observed, as a direct result of a significant reduction in the time- and axially averaged local wall friction velocity u_τ^+ . From the above discussion, it is understood that besides the influence of the curvature of elliptical pipe wall, the value of $\langle w \rangle^+$ is also directly affected

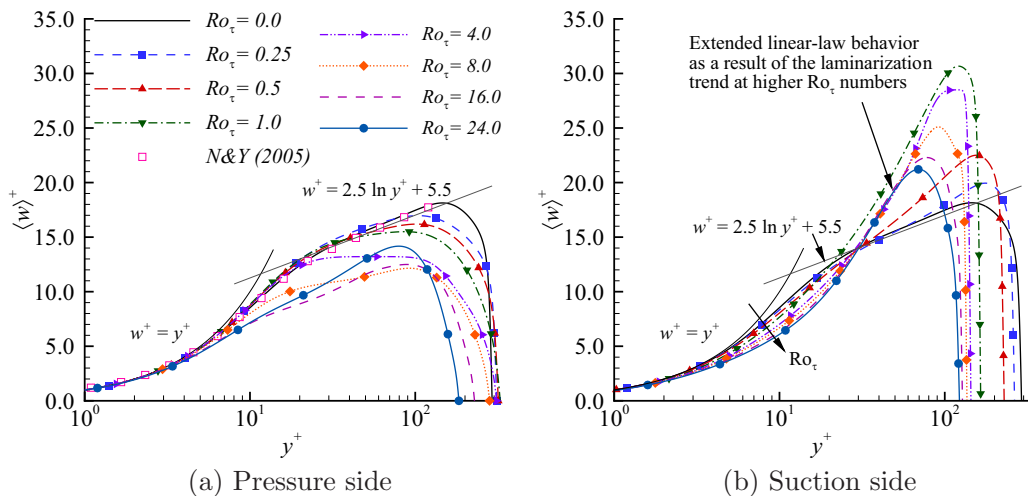


FIG. 8. Profiles of the mean axial velocity $\langle w \rangle^+$ displayed in the semilogarithmic wall coordinate system in the vertical plane ($\theta = 90^\circ$ or 270°) from (a) the pressure side and (b) the suction side at different rotation numbers. The profiles are nondimensionalized using the time- and axially averaged local friction velocity u_τ . Specifically, the value of $\langle w \rangle$ is nondimensionalized by u_τ^t and u_τ^b on the pressure and suction sides of the elliptical pipe, respectively. DNS data of Nikitin and Yakhot [19] (denoted as “N&Y (2005)”) are also presented for the purpose of comparison. The thin black lines represent the classical law-of-the-wall based on the two-layer boundary-layer model of von Kármán for a circular pipe flow. The arrow indicates a monotonic trend with an increasing Ro_τ .

by not only the secondary flow induced by the Coriolis force shown in Fig. 5, but also the wall friction velocities on the pressure and suction sides (i.e., u_τ^t and u_τ^b , respectively) shown previously in Fig. 6(b). Figure 8(b) shows the mean axial velocity profile in the wall coordinate measured from the suction side. As the rotation number increases from $Ro_\tau = 0$ to 24.0, the profile of $\langle w \rangle^+$ decreases monotonically within the viscous sublayer such that the viscous sublayer becomes increasingly thicker. This monotonic trend shown in Fig. 8(b) is consistent with that in Fig. 7(a), both clearly indicating that as the rotation number increases, the magnitude of the mean axial velocity decreases monotonically and the extent of the viscous sublayer increases monotonically on the suction side of the elliptical pipe. Opposite of the pressure side, as shown in Fig. 5, low-momentum fluid is transported by the secondary flow from the suction side to the core turbulent region of the pipe, leading to a significant fall in the mean axial velocity, and therefore, an extended viscous sublayer. As is evident in Fig. 8(b), the trend of laminarization becomes increasingly apparent as the rotation number increases. At the highest rotation number tested (i.e., at $Ro_\tau = 24.0$), the entire profile of $\langle w \rangle^+$ features an extended linear law of the wall, and the logarithmic layer (which is characteristic of a turbulent boundary layer) vanishes completely. In the range $Ro_\tau \geq 1.0$, the peak magnitude of $\langle w \rangle^+$ falls monotonically, but the slope remains much greater than that predicted by the classical logarithmic law, illustrating the great influence of the Coriolis force and curved elliptical boundary on the velocity field, which leads to significant deviation from the familiar classical predictive model of von Kármán for a nonrotating turbulent boundary-layer flow in a circular pipe.

In the current literature of nonrotating elliptical pipe flows [19–21], the focus of study has been primarily on the profile of the axial velocity $\langle w \rangle^+$. It would be interesting to investigate also the characteristics of the mean vertical velocity $\langle v \rangle^+$ for both rotating and nonrotating elliptical pipe flows. To achieve this objective, Fig. 9 shows the profiles of the nondimensionalized mean vertical velocity $\langle v \rangle^+$ along the major (or x) axis of the elliptical pipe at different rotation numbers. Given the axial symmetry of the mean flow of the nonrotating case ($Ro_\tau = 0.0$), the value of $\langle v \rangle^+$ is

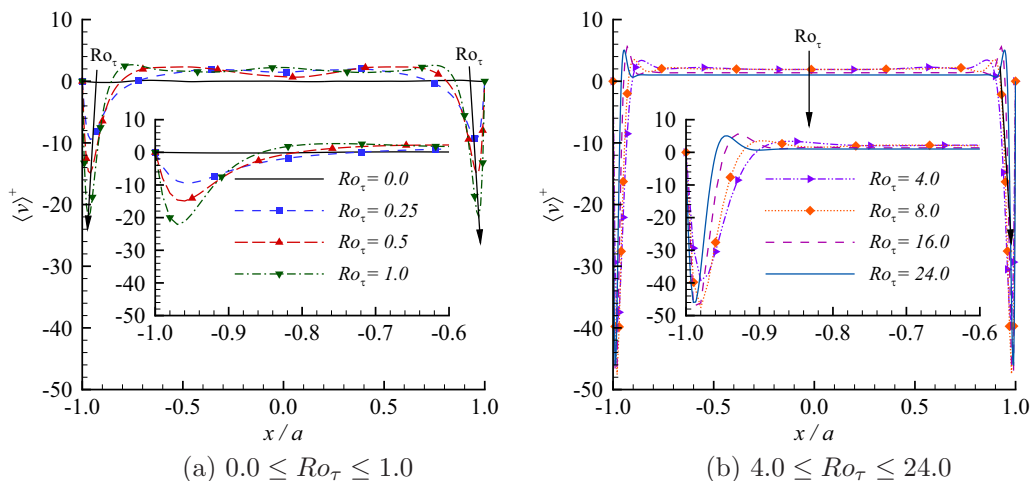


FIG. 9. Profiles of the mean vertical velocity $\langle v \rangle^+$ in the horizontal plane ($\theta = 0^\circ$ or 180°) along the major (x) axis. Given the significant differences in the magnitude between low and high rotation numbers, to have a clear view, the profiles of $\langle v \rangle^+$ are presented in two panels. (a) for $Ro_\tau = 0.0, 0.25, 0.5$, and 1.0 , and (b) for $4.0, 8.0, 16.0$, and 24.0 . The profiles are nondimensionalized using $u_{\tau 0S}$. Arrows indicate monotonic trends with an increasing rotation number Ro_τ .

trivial in Fig. 9(a). By contrast, owing to the system rotation, the profiles of all rotating cases shown in Figs. 9(a) and 9(b) are nontrivial, and feature two near-wall peaks along the major axis. As shown previously in Fig. 5, the symmetry of the mean flow field about the x axis at $Ro_\tau = 0$ is destroyed as soon as the system rotation is imposed due to the appearance of the y component of the Coriolis force ($2\Omega\langle w \rangle$). In the central region of the pipe, the occurrence of large secondary flow vortices (see Fig. 5) leads to positive values of $\langle v \rangle^+$ as the flow runs from the suction side to the pressure side of the pipe. Then the secondary flow splits and travels to the suction side along the two peripheral sides of the pipe, leading to a negative peak near either end of the major axis in Fig. 9. Although the mean vertical Coriolis force $2\Omega\langle w \rangle$ increases proportionally with the rotation number (the monotonic trend of $\langle w \rangle$ with Ro_τ has been demonstrated in Fig. 7), the profile of $\langle v \rangle^+$ does not necessarily vary monotonically with an increasing rotation number as the pattern and strength of the mean secondary flow pattern are also influenced by the curved surface of the elliptical pipe. Nevertheless, as is shown in Figs. 9(a) and (b), the magnitude of the near-wall peaks does increase monotonically in magnitude in the range $Ro_\tau \leq 8.0$. The trends and near-wall peaks of the mean vertical velocity $\langle v \rangle^+$ shown in Fig. 9 further influence the profiles of the mean axial velocity $\langle w \rangle^+$ (shown in Fig. 7(b) through the axial Coriolis force component $-2\Omega\langle v \rangle$).

C. Turbulence statistics

Figure 10 compares the contours of the nondimensionalized turbulence kinetic energy (TKE) (defined as $k^+ = \langle u_i u_i \rangle^+ / 2$) at four different rotation numbers. At $Ro_\tau = 0.0$, the contour is symmetric about the central horizontal plane (located at $y/b = 0$), but this quickly changes as the rotation number increases to $Ro_\tau = 0.25$. As shown previously in Fig. 5, as soon as the system rotation is imposed, secondary flows are altered in the cross-stream plane, which transport fluid from the suction side of the pipe toward the pipe center, and push the high TKE flow on the pressure side of the elliptical pipe closer to the top wall, a pattern that is evident in Fig. 10. On the suction side of the pipe, however, the TKE magnitude decreases due to the transport of viscously retarded fluid near the wall along the periphery as a result of the induced cross-stream secondary flow. At $Ro_\tau = 4.0$, laminarization has set in throughout the suction side of the pipe, due to a great reduction

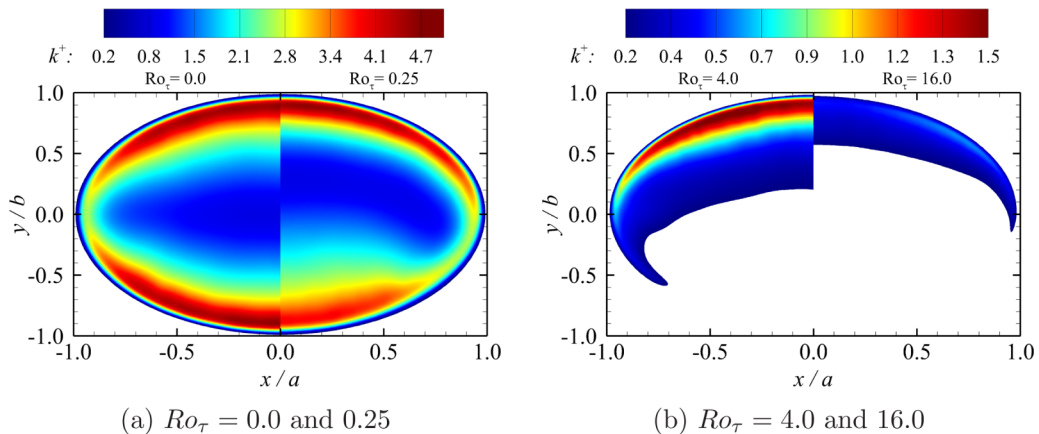


FIG. 10. Contours of turbulent kinetic energy k^+ nondimensionalized using $u_{\tau 0S}^2$ for cases of $Ro_\tau = 0.0, 0.25, 4.0,$ and 16.0 (left to right) in the cross-stream plane. Contours corresponding to TKE levels below $k^+ = 0.2$ are clipped to clearly show the propagation of laminarization.

of the mean velocity gradient near the bottom wall [see Fig. 7(a)] which subsequently reduces the TKE production rate (P_{ij} , to be studied later in this section). On the pressure side, the levels of TKE also decrease compared to that at $Ro_\tau = 0.25$. The trend toward laminarization continues, and at $Ro_\tau = 16.0$, a full laminarization state is almost reached, as the peak TKE level on the pressure side has reduced by as much as 87% compared to that at $Ro_\tau = 0.0$. At this high rotation number, laminarization spreads from the suction side of the pipe toward its pressure side and then from its center toward its two sides. At the highest rotation number tested ($Ro_\tau = 24.0$), the TKE level reduces to zero, as the flow has become completely laminarized.

Figure 11 shows the effect of system rotation on the profiles of the four nontrivial components of the Reynolds stresses $\langle w'w' \rangle^+, \langle u'u' \rangle^+, \langle v'v' \rangle^+$, and $\langle v'w' \rangle^+$ along the minor axis. The profiles of $\langle u'v' \rangle^+$ and $\langle u'w' \rangle^+$ are zero identically along the minor axis, and therefore, not presented here. Clearly, at $Ro_\tau = 0.0$, the profiles of all these Reynolds normal and shear stress components are symmetrical about the axial center. As soon as the system rotation is imposed, the symmetry is destroyed by the Coriolis force. A general feature is that the values of all these Reynolds stress components decrease monotonically near the suction side of the elliptical pipe as the rotation number increases from $Ro_\tau = 0.0$ to 24.0 . At $Ro_\tau = 24.0$, the values of these Reynolds stress components are zero on both suction and pressure sides of the elliptical pipe, clearly indicating a state of complete laminarization. From Fig. 11(a), it is seen that the peak of $\langle w'w' \rangle^+$ on the suction side not only decreases monotonically in magnitude but also moves toward the pressure side of the pipe as the rotation number increases. The drifting of the peak position of $\langle w'w' \rangle^+$ with an increasing rotation number is consistent with the trend of k^+ shown in Fig. 10. In fact, this trend is general and can also be observed in the profiles of other Reynolds stress components shown in Figs. 11(b)–11(d). For instance, it is interesting to see in Fig. 11(b) that the dual-peak pattern is preserved in the profile of $\langle u'u' \rangle^+$ at all rotation numbers tested. However, as the rotation number increases, the values of both peaks of $\langle u'u' \rangle^+$ decrease, and the peak on the suction side drifts toward the pressure side. This again clearly indicates that as the rotation number increases, the TKE drops more rapidly on the suction side than on the pressure side, and the boundary layer becomes increasingly thicker and thinner on the suction and pressure sides, respectively (see also Fig. 7). It is also interesting to observe an increase in the magnitudes of $\langle u'u' \rangle^+, \langle v'v' \rangle^+$ and $\langle v'w' \rangle^+$ on the pressure side of the pipe at $Ro_\tau = 8.0$ in Figs. 11(b), 11(c) and 11(d). This behavior of Reynolds stresses is qualitatively similar to that observed by Fang *et al.* [16] in their study of spanwise-rotating square duct flows. The variations of magnitude of these Reynolds stresses are related to their

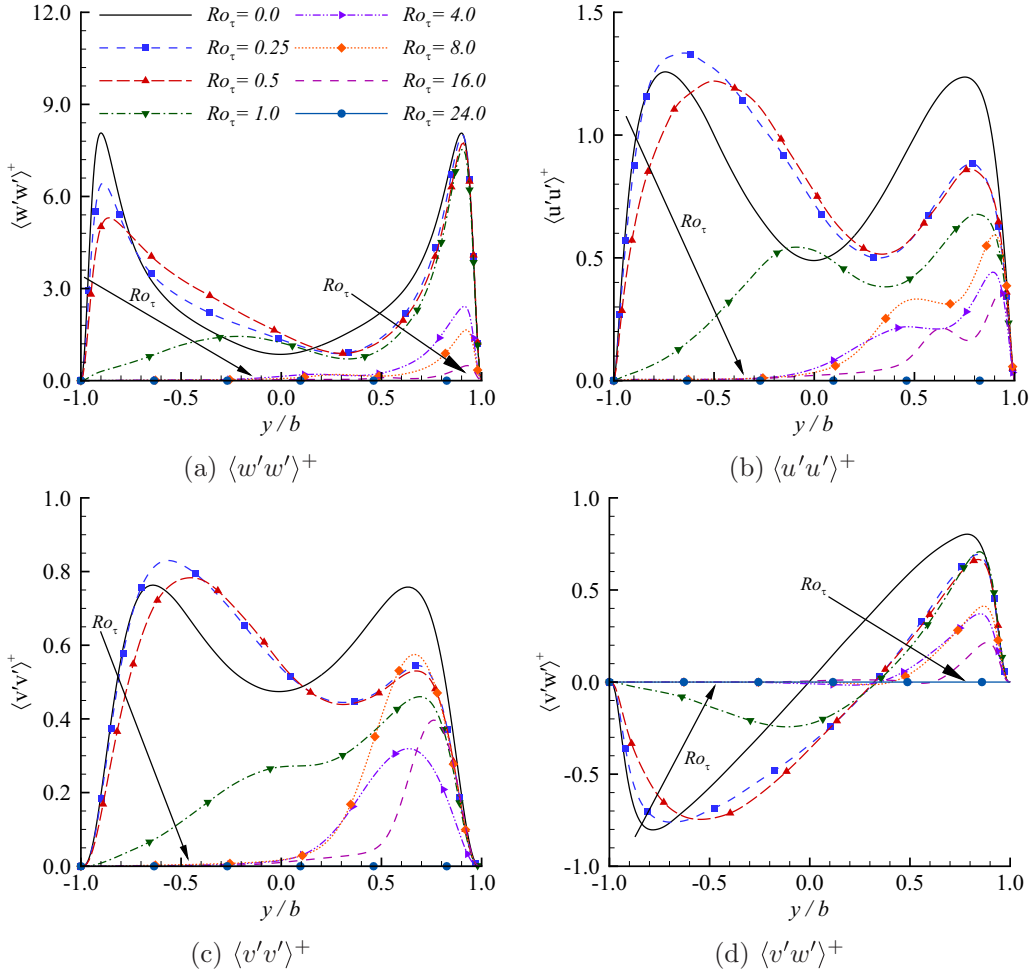


FIG. 11. Profiles of Reynolds normal and shear stresses nondimensionalized using $u_{\tau 0S}^2$ along the pipe minor axis (for $\theta = 90^\circ$ or 270°) at $Ro_\tau = 0.0, 0.25, 0.5, 1.0, 4.0, 8.0, 16.0,$ and 24.0 . An arrow indicates a monotonic trend with an increasing Ro_τ .

turbulent production term (P_{ij}), whose value is proportional to the mean velocity gradient. From Fig. 7(a), it is clear that as the rotation number increases, the boundary layer thickness on the suction side of the pipe increases, and in consequence, the mean velocity gradient in the y direction decreases which further leads to a reduction in the TKE production rate.

The effects of imposed system rotation on the profiles of nondimensionalized Reynolds stresses $\langle w'w' \rangle^+$, $\langle u'u' \rangle^+$, $\langle v'v' \rangle^+$ and $\langle u'w' \rangle^+$ along the major axis (or x axis) are shown in Fig. 12. The identified monotonic trends in these profiles with an increasing rotation number are indicated using arrows in the figure. Because both Coriolis force components are symmetrical about the central vertical plane (located at $x/a = 0$, see Fig. 1), the profiles are symmetrical for the Reynolds normal stresses and anti-symmetrical for the Reynolds shear stress about the about the central vertical plane at all rotation numbers (for $0 \leq Ro_\tau \leq 24.0$). This is in sharp contrast to the profiles of Reynolds stresses along the minor axis shown previously in Fig. 11, which become asymmetrical as soon as the system rotation is imposed (if $Ro_\tau \neq 0.0$). By comparing Fig. 12 with Fig. 11, it is interesting to observe that the profiles of Reynolds stresses exhibit more complex patterns along the major axis than along the minor axis for the nonrotating flow case at $Ro_\tau = 0.0$. For instance, at $Ro_\tau = 0.0$,

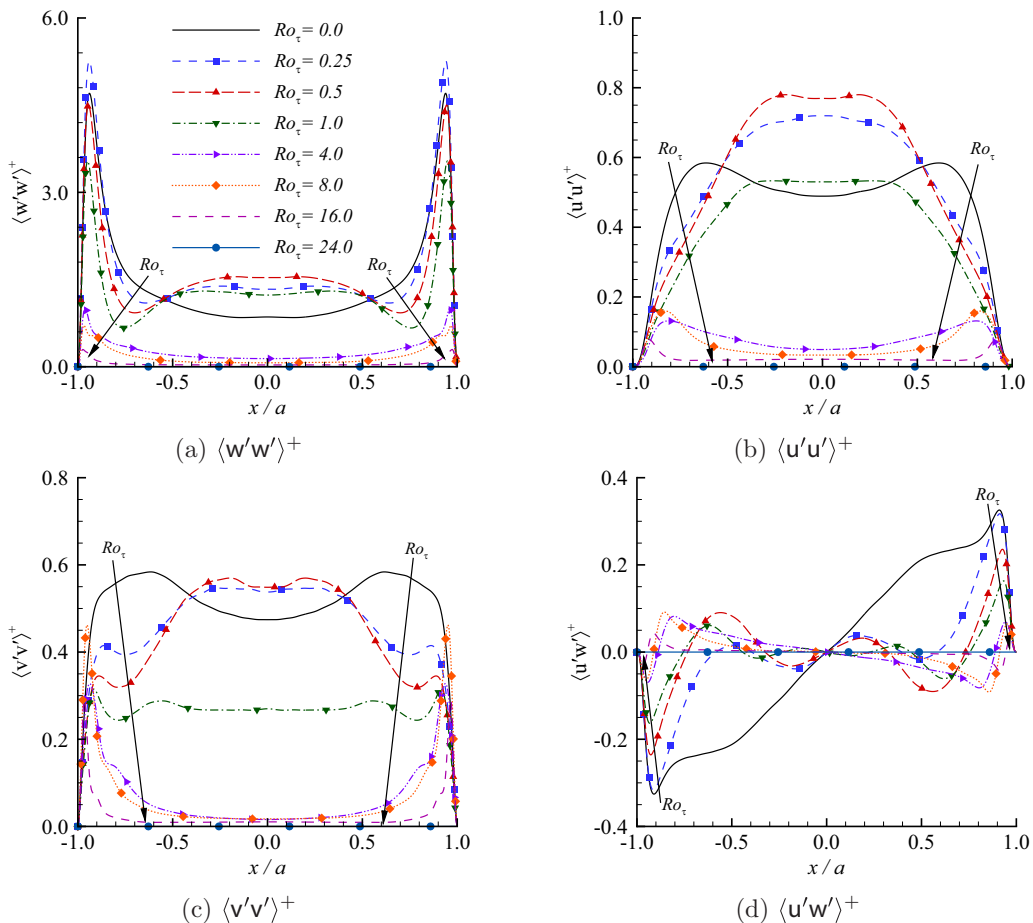


FIG. 12. Profiles of Reynolds normal and shear stresses nondimensionalized using $u_{\tau 0s}^2$ along the pipe major axis (for $\theta = 0^\circ$ or 180°) at $Ro_\tau = 0.0, 0.25, 0.5, 1.0, 4.0, 8.0, 16.0,$ and 24.0 . An arrow indicates a monotonic trend with an increasing Ro_τ .

the profile of $\langle v'w' \rangle^+$ shown in Fig. 11(d) is qualitatively similar to that of a turbulent plane channel flow, which features a linear Reynolds shear stress profile in the central region between the two near-wall peaks. However, as shown in Fig. 12(d), although the profile shape of $\langle u'w' \rangle^+$ is linear in the core turbulent region, this feature is not preserved close to the near-wall peaks. From Fig. 5, it is clear that the secondary-flow pattern is different around the ends of the major axis (for $\theta = 0^\circ$ or 180°) from those around the minor axis (for $\theta = 90^\circ$ or 270°). Owing to the significant difference in the surface curvature between the ends of the major and minor axes, the profile shapes of $\langle v'w' \rangle^+$ [along the minor axis shown in Fig. 11(d)] and $\langle u'w' \rangle^+$ [along the major axis shown in Fig. 12(d)] are considerably different.

The appearance of secondary flows (see Fig. 5) has a significant impact on the distribution of momentum in the cross-stream plane, which transport high TKE fluid from the suction side of the pipe to the center of the pipe at low rotation numbers in the range $0.25 \leq Ro_\tau \leq 0.5$, resulting in an initial increase in the magnitude of these Reynolds stress components in the central region of the major axis, a process that is evidenced by the behavior shown in the contours of TKE (Fig. 10). As the rotation number further increases to the range of $Ro_\tau \geq 1.0$, the effect of laminarization strengthens, and low TKE fluid is carried by the secondary flow from the suction side to the pipe

TABLE I. Nonzero components of the Coriolis term C_{ij} .

ij	22	23	33
C_{ij}	$4\Omega\langle v'w' \rangle$	$-2\Omega(\langle v'v' \rangle - \langle w'w' \rangle)$	$-4\Omega\langle v'w' \rangle$

center, which accounts for the decreasing trend observed in Fig. 12 for all normal Reynolds stress components in the central region in this rotation number range. Another common feature of these Reynolds stress components lies in the migration of the near-wall peaks toward the sidewalls in the rotation number range of $0.25 \leq \text{Ro}_\tau \leq 24.0$, occurring in response to the increasing wall-normal axial velocity gradient at the ends of the major axis [see Figs. 5(b) and 7(b)]. As the rotation number continues to increase, the spread of laminarization from the suction side of the pipe enhances, and eventually, the flow becomes fully laminarized and all Reynolds normal and shear stress values become trivial at $\text{Re}_\tau = 24.0$. The process of reduction in the magnitudes of Reynolds stresses along the major axis with an increasing rotation number shown in Fig. 12 is also associated with the growth of the TP region shown previously in Figs. 5 and 7(b). Within a TP region, $\partial\langle w \rangle / \partial x \approx 0$ holds. The production rate P_{ij} of these Reynolds stresses is strongly dependent on the mean axial velocity gradient in the x direction. As the TP region intensifies and expands with an increasing rotation number, the axial velocity gradient in the x direction approaches zero throughout the center of the pipe, reducing increasingly the production rates of these Reynolds stresses along the major axis.

To develop a deeper understanding of the trends of the Reynolds stress profiles along the minor axis, it is useful to further investigate their budget balances. The transport equation of Reynolds stresses is given as [16]

$$H_{ij} - P_{ij} - \Pi_{ij} + \varepsilon_{ij} - D_{ij} - C_{ij} = 0, \quad (3)$$

where H_{ij} , P_{ij} , Π_{ij} , ε_{ij} , D_{ij} , and C_{ij} are the convection, production, pressure-strain, viscous dissipation, diffusion, and Coriolis terms, respectively, defined as

$$H_{ij} = \langle u_k \rangle \frac{\partial \langle u'_i u'_j \rangle}{\partial x_k}, \quad (4)$$

$$P_{ij} = -\langle u'_i u'_k \rangle \frac{\partial \langle u_j \rangle}{\partial x_k} - \langle u'_j u'_k \rangle \frac{\partial \langle u_i \rangle}{\partial x_k}, \quad (5)$$

$$\Pi_{ij} = \frac{1}{\rho} \left\langle p' \left(\frac{\partial u'_i}{\partial x_j} + \frac{\partial u'_j}{\partial x_i} \right) \right\rangle, \quad (6)$$

$$\varepsilon_{ij} = 2\nu \left\langle \frac{\partial u'_i}{\partial x_k} \frac{\partial u'_j}{\partial x_k} \right\rangle, \quad (7)$$

$$D_{ij} = -\frac{\partial \langle u'_i u'_j u'_k \rangle}{\partial x_k} - \frac{1}{\rho} \frac{\partial}{\partial x_k} (\langle p' u'_j \rangle \delta_{ik} + \langle p' u'_i \rangle \delta_{jk}) + \nu \frac{\partial^2 \langle u'_i u'_j \rangle}{\partial x_k \partial x_k}, \quad (8)$$

$$C_{ij} = -2\Omega (\langle u'_i u'_k \rangle \epsilon_{kj1} + \langle u'_j u'_k \rangle \epsilon_{ki1}). \quad (9)$$

The profiles of these budget terms along the pipe minor axis are shown in Figs. 13, 14, and 15 for $\langle w'w' \rangle$, $\langle v'w' \rangle$, and $\langle v'v' \rangle$, respectively. For convenience, all nonzero Coriolis term components resulted from the imposed system rotation are given in Table I. Clearly, the effect of the Coriolis term is the opposite in the budgets of $\langle v'v' \rangle$ and $\langle w'w' \rangle$, as the identity $C_{22} \equiv -C_{33}$ holds strictly. This indicates that the effect of the Coriolis force is to shift turbulence energy between Reynolds normal stress components $\langle v'v' \rangle$ and $\langle w'w' \rangle$. Furthermore, the Coriolis effect on the budget of the Reynolds shear stress $\langle v'w' \rangle$ is dependent entirely on the balance between the two Reynolds normal stresses $\langle v'v' \rangle$ and $\langle w'w' \rangle$, simply because $C_{23} \equiv -2\Omega(\langle v'v' \rangle - \langle w'w' \rangle)$.

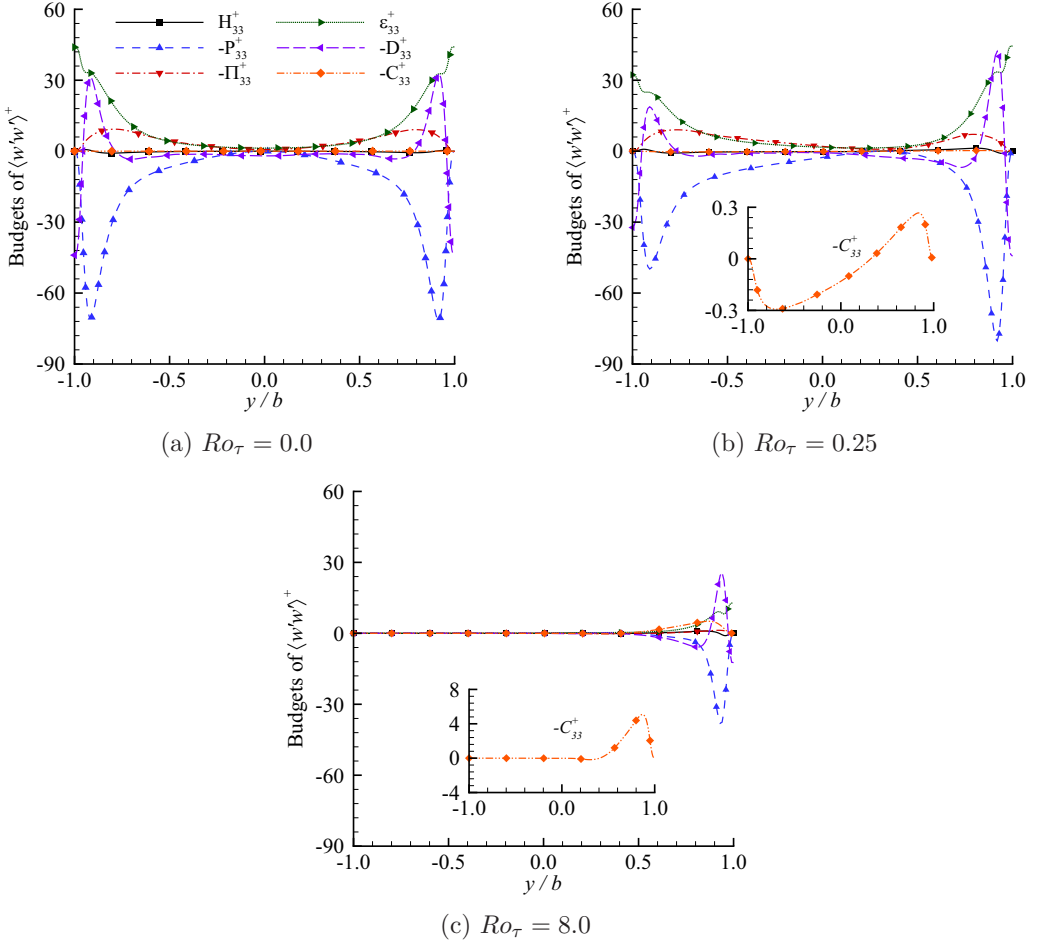


FIG. 13. Profiles of the budget terms of $\langle w'w' \rangle^+$ along the minor axis (nondimensionalized by $u_{\tau 0S}^3/b$) at $Ro_\tau = 0.0, 0.25$, and 8.0 .

Figure 13 shows the budget balance of $\langle w'w' \rangle^+$ at three different rotation numbers. For the nonrotating flow at $Ro_\tau = 0.0$, the Coriolis term is zero identically, i.e., $C_{33}^+ = 0$, and the convection term H_{33}^+ is trivial. The budget balance is dominated by the turbulent production term P_{33}^+ , counterbalanced by molecular dissipation ε_{33}^+ , diffusion term D_{33}^+ , and pressure-strain term Π_{33}^+ , especially in the near-wall region. A comparison of Figs. 13(a) and (b) reveals that the effects of system rotation on the budget balance of $\langle w'w' \rangle^+$ are apparent even though the rotation number is as low as $Ro_\tau = 0.25$. As is clear in Fig. 13(b), the profiles of budget terms are no longer symmetrical in the vertical direction along the y axis under the influence of Coriolis forces. The system rotation leads to a significant reduction (by 29.6%) in the peak value of the production term P_{33}^+ on the suction side of the flow. The magnitudes of the peaks of the dissipation and diffusion terms also decrease, by 26.5% and 40.0%, respectively. At this low rotation number, the Coriolis term C_{33}^+ acts as a small energy source and sink on the suction and pressure sides of the pipe, respectively. In general, the contribution from the Coriolis term C_{33}^+ is very small at $Ro_\tau = 0.25$. For instance, at its peak, the Coriolis term provides only 0.6% of the energy of the production term at its peak on the suction side. From the previous discussion, it is understood that the Coriolis forces induced by the system rotation have a significant impact on the turbulence field in terms of the instantaneous

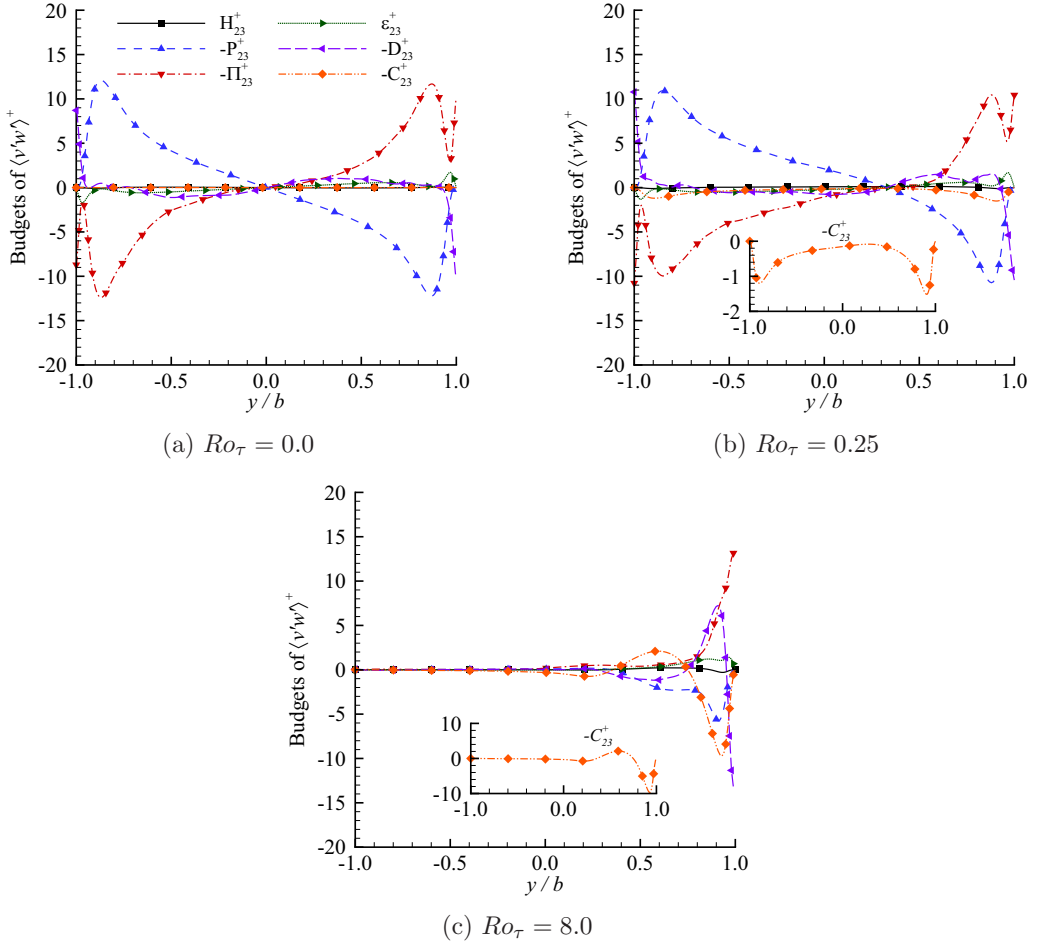


FIG. 14. Profiles of the budget terms of $\langle v'w' \rangle^+$ along the minor axis (nondimensionalized by $u_{\tau 0S}^3/b$) at $Ro_\tau = 0.0, 0.25$, and 8.0 .

and mean flows, and Reynolds stresses, which further significantly influence the budget balance of the Reynolds stresses through Eqs. (4)–(9). However, the influence of system rotation directly embodied by the Coriolis term C_{33}^+ on the budget balance of Reynolds stress $\langle w'w' \rangle^+$ can be very limited at a low rotation number. From Fig. 13(c), it is seen that as the rotation number increases to $Ro_\tau = 8.0$, the profiles of the budget terms become completely asymmetrical about the pipe center. The magnitude of the Coriolis term C_{33}^+ has also increased, and its peak value is approximately 13.4% of that of the turbulent production term P_{33}^+ on the pressure side of the elliptical pipe at $Ro_\tau = 8.0$. Apparently, laminarization has occurred on the suction side of the elliptical pipe, and partly spread to the pressure side at this rotation number. The trend of laminarization with an increasing rotation number can be also judged by observing the variation of the peak magnitude of the turbulent production term P_{33}^+ , which shows a 46.9% reduction at $Ro_\tau = 8.0$ from that of the nonrotating flow (at $Ro_\tau = 0.0$).

Figures 14(a)–14(c) compare the budget balances of $\langle v'w' \rangle^+$ at three different rotation numbers. Clearly, for the nonrotating case ($Ro_\tau = 0$), the profiles are symmetrical about the pipe center in the vertical direction. However, as soon as the spanwise system rotation is imposed, the Coriolis term $-C_{23}^+$ appears, and the symmetry in the profiles of the budget terms is destroyed. At the lower

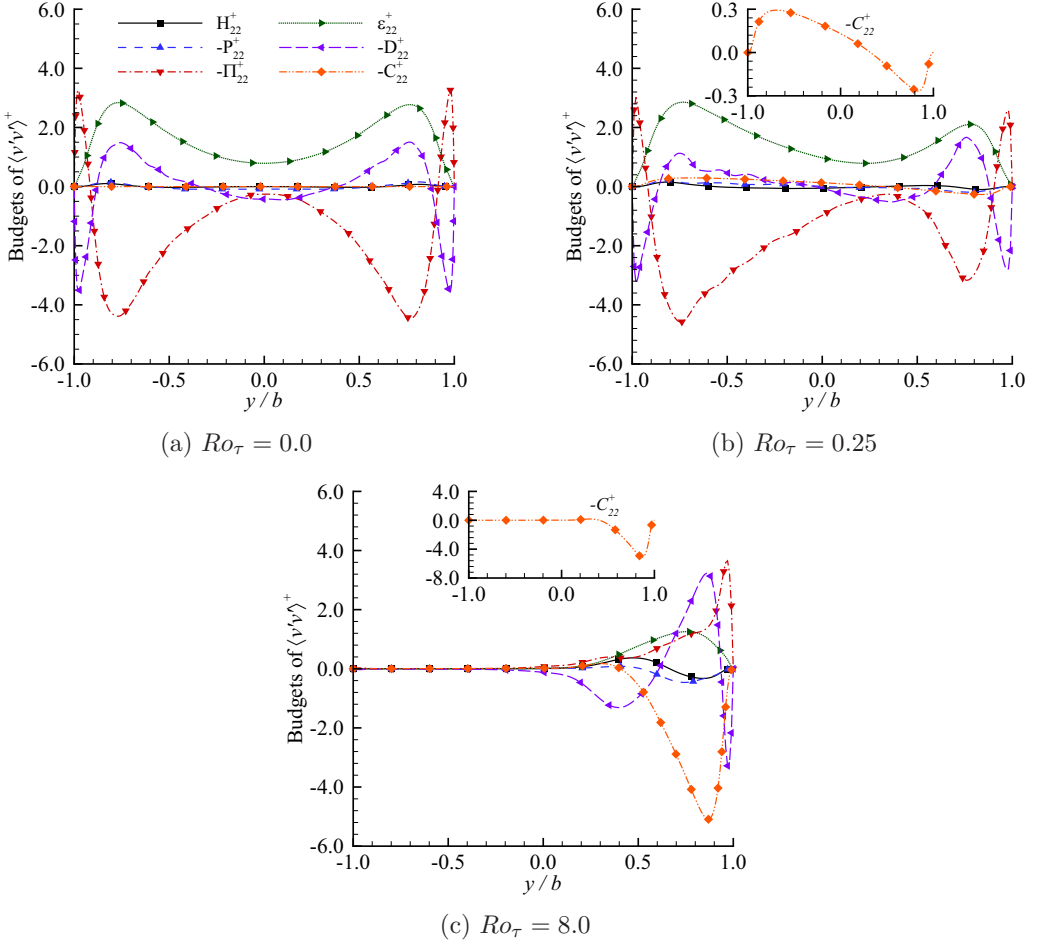


FIG. 15. Profiles of the budget terms of $\langle v'v' \rangle^+$ along the minor axis (nondimensionalized by $u_{\tau 0S}^3/b$) at $Ro_\tau = 0.0, 0.25$, and 8.0 .

rotation numbers (for $Ro_\tau = 0$ and 0.25), the turbulent production term P_{23}^+ is primarily balanced by the pressure-strain term Π_{23}^+ . As the rotation number increases, the Coriolis term C_{23}^+ increases in magnitude, and laminarization occurs on the suction side of the elliptical pipe. In fact, at $Ro_\tau = 8.0$, the peak magnitude of the production term P_{23}^+ is 47.2% of that of the nonrotating elliptical pipe flow case. As shown clearly in Fig. 14(c), the Coriolis term C_{23}^+ becomes an important source of energy in the near-wall region, transporting energy into $\langle v'w' \rangle^+$ at a rate of $-2\Omega(\langle v'v' \rangle^+ - \langle w'w' \rangle^+)$ (see Table D). In fact, the magnitude of C_{23}^+ has become larger than that of P_{23}^+ on the pressure side of the elliptical pipe, and the budget balance is dominated by C_{23}^+ , P_{23}^+ , D_{23}^+ , and Π_{23}^+ . The significant additional energy brought in by C_{23}^+ coincides with the increase in the peak value of $\langle v'w' \rangle^+$ at $Ro_\tau = 8.0$ shown previously in Fig. 11(d). From Fig. 14(c), it is interesting to observe that in the region $0.35 < y/b < 0.75$, where the value of $\langle v'v' \rangle^+$ surpasses that of $\langle w'w' \rangle^+$ [see Figs. 11(a) and 11(c)], the Coriolis term becomes negatively valued (because $C_{23}^+ = -2\Omega(\langle v'v' \rangle^+ - \langle w'w' \rangle^+) \leq 0$), and so it acts as an energy sink for Reynolds shear stress $\langle v'w' \rangle^+$.

Figure 15 shows the effect of system rotation on the budget balances of $\langle v'v' \rangle^+$. As is evident in Fig. 15(a), the budget balance of $\langle v'v' \rangle^+$ is dominated by the pressure-strain term Π_{22}^+ , which is counterbalanced by the molecular dissipation term ϵ_{22}^+ and the diffusion term D_{22}^+ in the core

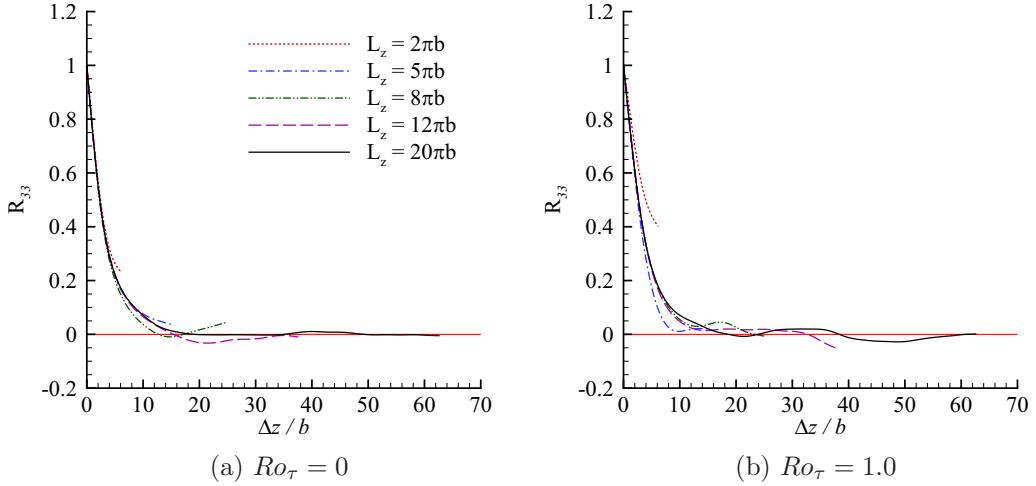


FIG. 16. Two-point autocorrelation coefficients of the axial velocity fluctuations along the axial direction of the pipe at wall-normal position $y^+ = 14.1$ on the pressure side of the pipe in the central vertical plane ($\theta = 90^\circ$ or 270°) for nonrotating and rotating elliptical pipe flows of $Ro_\tau = 0$ and 1.0. The value of R_{33} is obtained by performing independent DNS based on various domain sizes (in the range $2\pi b \leq L_z \leq 20\pi b$) at both rotation numbers.

turbulent region of the elliptical pipe flow. By contrast, the magnitude of the turbulent production term P_{22}^+ is relatively small at $Ro_\tau = 0.0$, a feature that is considerably different from those of $\langle w'w' \rangle^+$ and $\langle v'w' \rangle^+$ shown previously in Figs. 13(a) and 14(a). In a similar fashion as seen in Fig. 14, the profiles of the budget terms are symmetric and the separation point between the suction and pressure sides is at the elliptical pipe center (or $y/b = 0$). As soon as the rotation number increases slightly from $Ro_\tau = 0.0$ to 0.25, the profiles become asymmetric, and the separation point shifts from the pipe center to the pressure side at approximately $y/b = 0.3$. As shown in Fig. 15(b), the magnitude of the pressure-strain term Π_{22}^+ increases on the suction side of the pipe at $Ro_\tau = 0.25$, a pattern that is consistent with that of $\langle v'v' \rangle^+$ shown in Fig. 11(c) at the same rotation number. Also at $Ro_\tau = 0.25$, the Coriolis term C_{22}^+ appears, which acts as a minor energy sink on the suction side and a minor energy source on the pressure side. This behavior of the Coriolis term is the exact opposite of the Coriolis term of $\langle w'w' \rangle^+$ shown previously in Fig. 13(b), simply because $C_{22}^+ \equiv -C_{33}^+$. At $Ro_\tau = 8.0$ as shown in Fig. 15(c), it is interesting to observe that the magnitude of the Coriolis term C_{22}^+ increases drastically, and becomes the dominant source of energy for $\langle v'v' \rangle^+$ on the pressure side of the elliptical pipe. This event coincides with a significant increase in the peak magnitude of $\langle v'v' \rangle^+$ at the same rotation number observed in Fig. 11(c). From Fig. 15(c), it is clear that the Coriolis term is counterbalanced primarily by the pressure strain terms Π_{22}^+ and diffusion term D_{22}^+ on the pressure side of the pipe. Finally, as a consequence of the induced secondary flow in the positive y direction, the production term P_{22}^+ also increases in magnitude and becomes a minor source of energy for the Reynolds normal stress component $\langle v'v' \rangle^+$.

Figures 16 compares the two-point autocorrelation coefficients $R_{33}(\Delta z)$ of the axial velocity fluctuations obtained by performing independent DNS based on various domain sizes (in the range $2\pi b \leq L_z \leq 20\pi b$) for both nonrotating and rotating elliptical pipe flows of $Ro_\tau = 0$ and 1.0. Here, the two-point autocorrelation coefficient is defined as

$$R_{33}(\Delta z) = \frac{\langle w'(x, y, z, t)w'(x, y, z + \Delta z, t) \rangle}{\langle w'(x, y, z, t)w'(x, y, z, t) \rangle}. \quad (10)$$

The calculation of the R_{33} value is conducted for wall-normal position $y^+ = 14.1$ on the pressure side of the pipe in the central vertical plane ($\theta = 90^\circ$ or 270°). The reason this particular wall-normal position is selected is that the magnitude of $\langle w'w' \rangle^+$ peaks at this position. As is evident in Fig. 16, the value of R_{33} of the shortest pipe length $L_z = 2\pi b$ ends up well above zero in both nonrotating and rotating flow cases, clearly indicating that axial computational domain is insufficient for capturing large axial turbulent eddy motions. As the pipe length increases to $L_z = 5\pi b$ and $8\pi b$, the cutoff value R_{33} becomes closer to zero, but the result is still not satisfactory. From Fig. 16, it is fair to say that a minimum domain size of $L_z \geq 12\pi b$ is needed to capture the most energetic axially elongated turbulence structures at both rotation numbers tested.

As is well known, both two-point autocorrelation coefficient and premultiplied spectrum are useful in a pipe length study, as they are counterpart of each other in a Fourier transformation. The pipe length analysis based on premultiplied spectra is precise in the sense that not only we know exactly the energy level of turbulence structures at each specific wavelength, but also we are able to diagnose the mode that corresponds to the characteristic length of the most energetic flow structures in an accurate manner. In the following, we will refine the analysis by studying the premultiplied spectrum of the axial velocity fluctuations, and draw the conclusion that the minimum pipe length must be kept at $L_z = 20\pi b$ to limit the energy leaking to one-third of its peak value at the cutoff wavelength.

Figure 17 compares the premultiplied spectra $k_z^+ \phi_{ii}^+$ (no summation convention is implied) of axial, wall-normal, and spanwise velocity fluctuations ($k_z^+ \phi_{33}^+$, $k_z^+ \phi_{22}^+$, and $k_z^+ \phi_{11}^+$) at location $y^+ = 14.1$ on the pressure side of the pipe, where the peak magnitude of $\langle w'w' \rangle^+$ occurs. Here, k_z represents the axial wavenumber, nondimensionalized as $k_z^+ = k_z \nu / u_{\tau 0 S}$, and ϕ_{11} , ϕ_{22} , and ϕ_{33} represent the axial energy spectra of the three fluctuating velocity components, nondimensionalized as $\phi_{ii}^+ = \phi_{ii} / (\nu u_{\tau 0 S})$. In Fig. 17, λ_z^+ represents the nondimensionalized axial wavelength (defined as $\lambda_z^+ = 2\pi / k_z^+$). Although the premultiplied spectra at various rotation numbers shown in Fig. 17 are all calculated based on a fixed pipe length of $L_z = 20\pi b$, and the cutoff wavelengths corresponding to shorter pipe lengths are indicated in panel (a) to show the energy levels. By comparing Figs. 17(a)–17(c), it is evident that the magnitude of the axial component $k_z^+ \phi_{33}^+$ is much greater than those of both $k_z^+ \phi_{22}^+$ and $k_z^+ \phi_{11}^+$, indicating that the axial velocity fluctuations make the greatest contribution to the TKE of the flow. Figure 17(a) shows an initial increase in the peak energy as the rotation number increases from $Ro_\tau = 0.0$ to 0.25. As the rotation number continues to increase from $Ro_\tau = 0.25$ to 24.0, the magnitude of $k_z^+ \phi_{33}^+$ decreases monotonically until it reaches zero for all wavelengths at $Ro_\tau = 24.0$, which is a reflection of the laminarization process. In the nonrotating case, the characteristic wavelength corresponding to the most energetic eddies, as indicated by the mode of $k_z^+ \phi_{33}^+$, is $\lambda_z^+ \approx 1260$. As the rotation number increases to $Ro_\tau = 1.0$, the mode changes to $\lambda_z^+ \approx 2820$, indicating that the Coriolis forces facilitate a significant initial growth in the axial characteristic length scale of the most energetic eddies. Because the TKE levels as represented by the magnitudes of $k_z^+ \phi_{11}^+$ and $k_z^+ \phi_{22}^+$ are much smaller than those represented by the axial component $k_z^+ \phi_{33}^+$, the variation in the magnitude of the nondimensionalized premultiplied spectrum is less dramatic in Figs. 17(b) and 17(c) than in Fig. 17(a). Still, some trends of $k_z^+ \phi_{11}^+$ and $k_z^+ \phi_{22}^+$ are consistent with those of $k_z^+ \phi_{33}^+$. As the rotation number increases from $Ro_\tau = 0.0$ to 4.0, the magnitudes of $k_z^+ \phi_{11}^+$ and $k_z^+ \phi_{22}^+$ decrease in general, and become trivial at $Ro_\tau = 24.0$, reflecting the trend of laminarization. However, as the rotation number increases from $Ro_\tau = 4.0$ to 16.0, there is an increase in the magnitudes of $k_z^+ \phi_{11}^+$ and $k_z^+ \phi_{22}^+$. This is due to the migration of the peaks of $\langle v'v' \rangle^+$ and $\langle u'u' \rangle^+$ toward the wall due to the induced secondary flow, which leads to a higher value of these Reynolds stress components at the probed location.

A further perusal of Figs. 17(a)–17(c) shows that the energy level at the cutoff wavelength is greater for the axial component at all rotation numbers than those for the wall-normal and spanwise components of the nondimensionalized premultiplied energy spectra. In the present study, the greatest amount of energy loss (relative to the peak value of the premultiplied spectrum) at the cutoff wavelength occurs at $Ro_\tau = 1.0$, where the percentage of TKE loss with respect to the peak value of $k_z^+ \phi_{33}^+$ was 33.7%. This indicates that only less than 33.7% of the peak energy

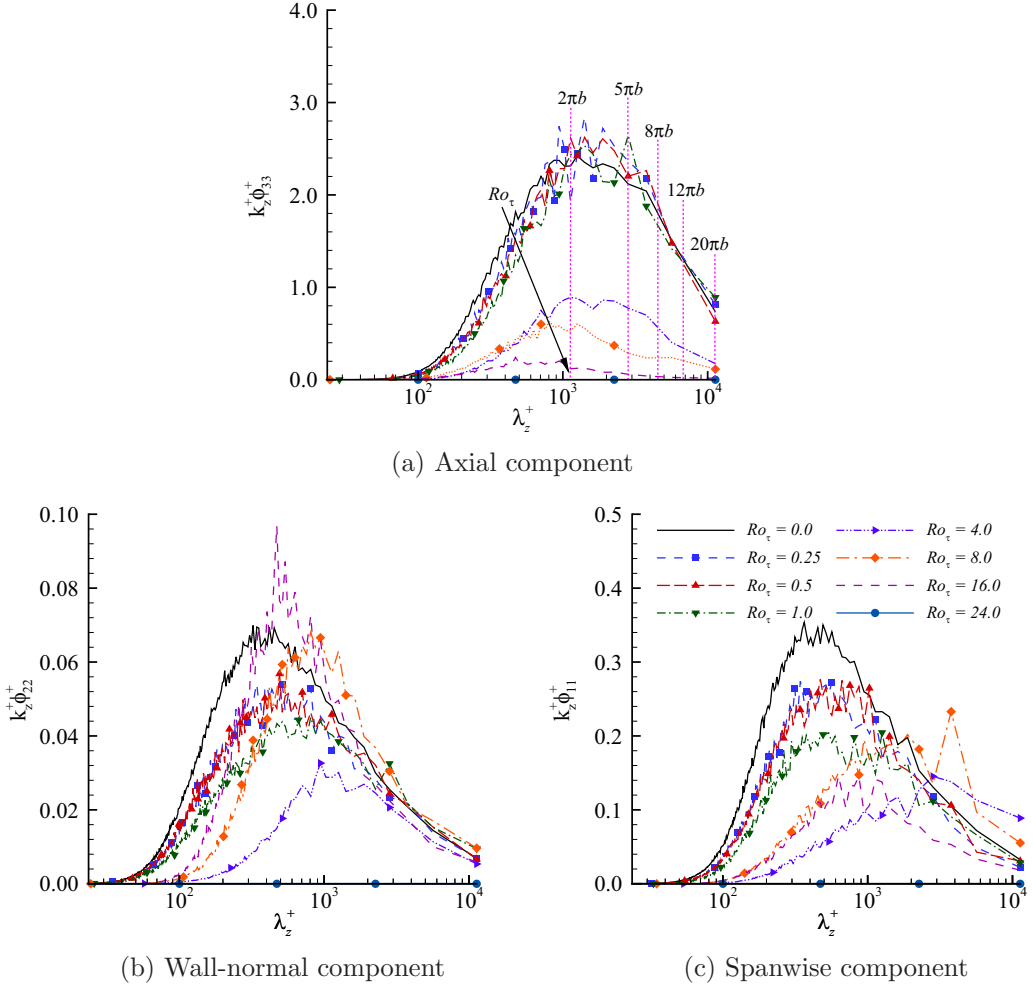


FIG. 17. Effect of spanwise system rotation on the premultiplied velocity spectra $k_z^+ \phi_{ii}^+$ nondimensionalized by $u_{\tau 0s}^2$ along the axial direction at wall-normal position $y^+ = 14.1$ on the pressure side of the pipe in the central vertical plane ($\theta = 90^\circ$ or 270°). The premultiplied spectra at various rotation numbers are all calculated based on a fixed pipe length of $L_z = 20\pi b$, and the cutoff wavelengths corresponding to shorter pipe lengths are indicated in panel (a). The arrows indicate monotonic trends as a result of an increasing rotation number.

remains uncaptured. This is a satisfactory result, which indicates that the elliptical pipe length is sufficiently long for catching not only the mode of the premultiplied spectra, but also the majority of the energy-containing eddy motions. By contrast, as shown in Fig. 17(a), a domain length of $L_z = 12\pi b$ would result in 48.3% of the peak energy being uncaptured at the cutoff wavelength, making it clear that a domain length of $L_z = 20\pi b$ is necessary to adequately capture the most energetic eddy motions, if the criterion is that the energy leaking the cutoff wavelength is limited to 1/3-rd of the peak value. It needs to be indicated that it is neither practical nor necessary to capture the premultiplied energy spectrum fully with 0% of spectrum leaking at the cutoff wavelength, either in a DNS or in a physical experiment, as this would require a use of an elliptical pipe of infinite length. In fact, the elliptical pipe length of $L_z = 20\pi b$ used in the present study is the longest in the current literature, which is four times that used in Nikitin and Yakhot [19], who conducted a DNS study of a nonrotating elliptical pipe flow at a similar Reynolds number.

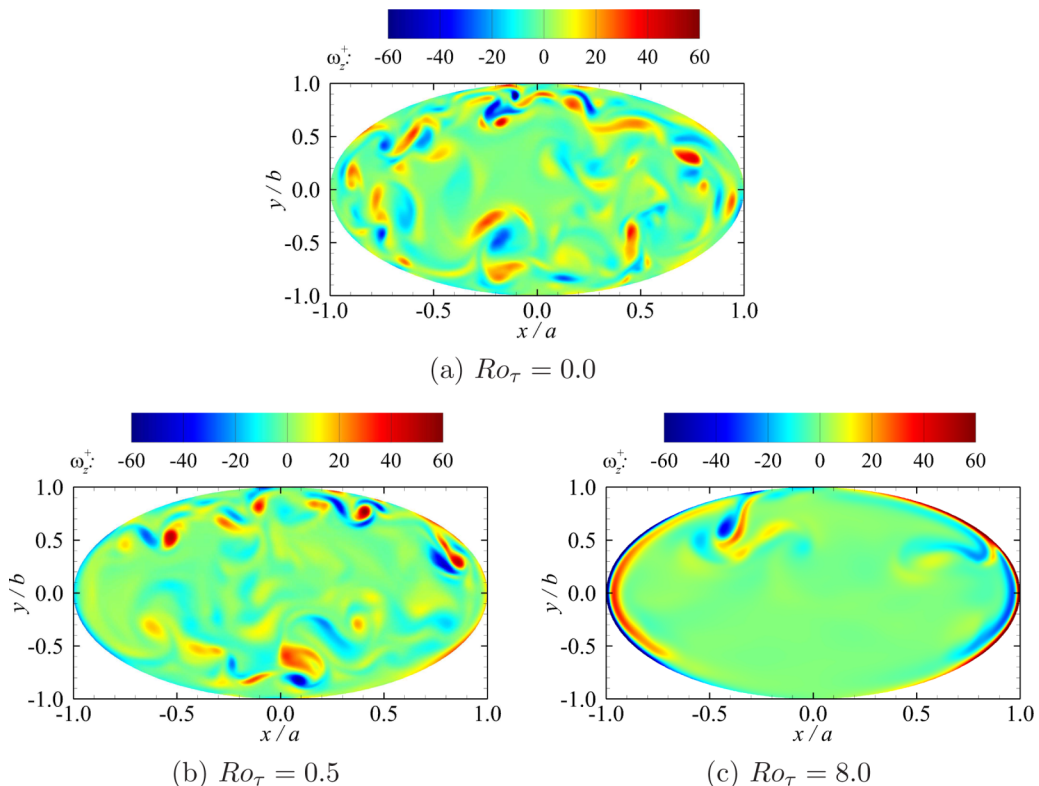


FIG. 18. Contours of instantaneous axial vorticity ω_z^+ nondimensionalized by $u_{\tau 0S}^2/\nu$ in cross-stream planes at different rotation numbers. All contours are extracted at the same time instant (at the beginning of the 41st LETOT of each simulation).

D. Flow structures

Figure 18 compares the instantaneous flows structures visualized using the axial vorticity ($\omega_z^+ = \partial u^+/\partial y^+ - \partial v^+/\partial x^+$) in a cross-stream plane at different rotation numbers. In the nonrotating case, Fig. 18(a) shows a relatively large number of counterrotating vortical pairs near the top and bottom walls of the pipe. As the rotation number increases to $Ro_\tau = 0.5$, the vortical structures on the suction side decrease in number. This is consistent with the laminarization trend observed in Fig. 11, which starts on the suction side of the elliptical pipe. On the pressure side of the flow, the vortical pairs are generally clustered closer to the wall as a result of the induced secondary flow in the positive y direction (see Fig. 5). Also at $Ro_\tau = 0.5$, strong narrow shear layers appear on both left and right sides of the elliptical pipe as a result of the induced secondary flow traveling from the pressure side to the suction side along the periphery of the pipe (see Fig. 5). These shear layers enhance significantly in strength as the rotation number further increases from $Ro_\tau = 0.5$ to 8.0. As is clear in Fig. 18(c), once the rotation number increases to $Ro_\tau = 8.0$, the number of vortices is greatly reduced, and they are mostly confined to the near-wall region of the pressure side of the pipe. The suction side shows a very low level of instantaneous vorticity ω_z^+ , as the flow has been laminarized considerably in this region.

The Coriolis forces induced by the system rotation dramatically alter turbulence structures of the flow. To demonstrate, the isosurfaces of vortical structures (visualized using the swirling strength, or the so-called λ_{ci} criterion following Zhou *et al.* [31] and Adrian [32]) are plotted for the cases of $Ro_\tau = 0.0, 0.5$ and 8.0 in Fig. 19. The contours on the plots are colored using the nondimensionalized elliptical radius r/R , where $r = \sqrt{x^2 + y^2}$ and $R = \sqrt{1/(\cos^2 \theta/a^2 + \sin^2 \theta/b^2)}$.

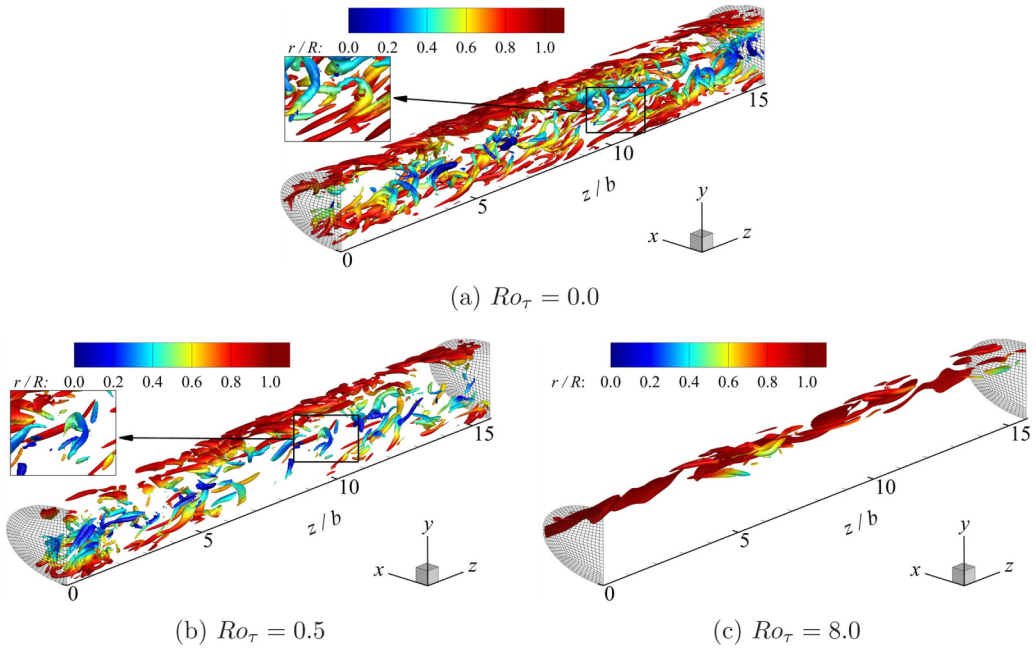


FIG. 19. Isosurfaces of instantaneous vortical structures (plotted by setting the swirling strength to $\lambda_{ci} = 1.0$) for the nonrotating ($Ro_\tau = 0.0$) and rotating ($Ro_\tau = 0.5$ and 8.0) cases. For clarity, only a quarter of the axial domain and one half of the cross-stream domain are shown. The contour colors indicate the nondimensionalized elliptical radius r/R . All instantaneous snapshots are extracted from the same time instant (at the beginning of the 41st LETOT of each simulation).

Figure 19(a) shows a cascade of hairpin structures symmetrically distributed on the top and bottom sides of the elliptical pipe at $Ro_\tau = 0.0$. By contrast, their presence is markedly reduced on the left and right sides of the pipe, suggesting that an increased degree of curvature close to the two ends of the major axis poses an impediment to the formation of these hairpin structures. A comparison of Figs. 19(a) and 19(b) reveals that, while hairpin structures are still present on both the suction and pressure sides of the pipe at $Ro_\tau = 0.5$, they become less populated and significantly shorter in the axial direction as the rotation number increases from $Ro_\tau = 0.0$ to 0.5 . This is due to the secondary flow pattern and the appearance of the Coriolis force in the positive y direction in response to the imposed system rotation (see Fig. 5), which lead to laminarization on the suction side of the pipe. From Fig. 19(c), it is clear that as the rotation number further increases to $Ro_\tau = 8.0$, the formation of coherent structures is greatly impeded also on the pressure side of the pipe and laminarization is seen to spread throughout its suction side. Furthermore, no complete hairpin structures are observed at this rotation number. At $Ro_\tau = 8.0$, the strength of the secondary flow is significantly enhanced (see Fig. 5), which pushes the existing coherent structures toward the pressure side of the pipe, inhibiting the normal bursting behavior of the flow, a mechanism that is essential for the formation and evolution of hairpin structures.

Figure 20 compares the near-wall streaks of the elliptical pipe flows of different rotation numbers at wall-normal distance $d^+ = 14.1$ along the elliptical periphery, where the wall coordinate is calculated based on ν and $u_{\tau 0S}$. The streaky structures are visualized using the instantaneous axial velocity fluctuations w'^+ . This particular location was chosen because the magnitude of $\langle w'w' \rangle^+$ peaks at this location (see Fig. 11). The blue and red patterns indicate low- and high-momentum streaks, respectively. For the nonrotating case shown in Fig. 20(a), the low and high-momentum streaks alternate along the peripheral direction, and furthermore, the streaks are similar between the

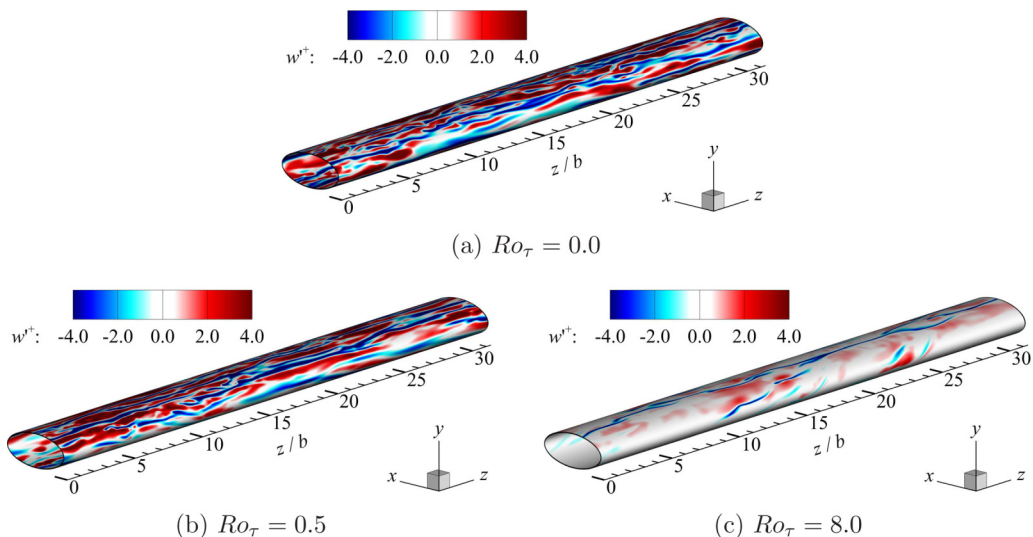


FIG. 20. Near-wall streaks visualized using the contours of instantaneous axial velocity fluctuation w'^+ (nondimensionalized using $u_{\tau 0S}$) at wall-normal distance $d^+ = 14.1$ along the periphery for $Ro_\tau = 0.0, 0.5,$ and 8.0 . For clarity, only half of the axial domain size is shown. All instantaneous snapshots are extracted from the same time instant (at the beginning of the 41st LETOT of each simulation).

top and bottom walls of the elliptical pipe. Near the sidewalls (close to the two ends of the major axis), however, a reduction is observed in the strength of low- and high-momentum streaks as a result of the increased wall curvature, coinciding with the reduction in the number of hairpin structures in the same region observed previously in Fig. 19(a). By comparing Figs. 20(a)–20(c), it is clear that as the rotation number increases, the strength of near-wall streaks decreases as laminarization significantly spreads from the suction side to the pressure side of the elliptical pipe (see Fig. 10(b)). Further comparison of Figs. 20(a) and 20(c) reveals that the axial length scale of the streaky structures is also significantly reduced at $Ro_\tau = 8.0$ when compared to that of the nonrotating case ($Ro_\tau = 0.0$). This coincides with the previously observed behavior of the premultiplied axial spectra of the axial velocity fluctuations in Fig. 17(a), as well as the disappearance of hairpin structures in Fig. 19(c).

To develop deeper insights into the physical features observed in Figs. 19 and 20, the joint probability density functions (JPDFs) of w' and $-v'$, are calculated. Figure 21 compares the JPDF patterns of the turbulence field at the same three rotation numbers and wall-normal position as in Figs. 19 and 20. In the calculation of JPDFs, $-v'$ is considered simply because the wall coordinate is measured from the top (or pressure) side along the minor axis of the elliptical pipe. Figure 21(a) displays the JPDF of w' and $-v'$ for the nonrotating case, which shows that the fluctuations of the axial velocity (w') synchronize well with those of the wall-normal velocity ($-v'$) and preferentially occur in the Q2 and Q4 quadrants. Events in these quadrants are known as ejections (featuring $-v' > 0$ and $w' < 0$) and sweeps (featuring $-v' < 0$ and $w' > 0$), respectively, and their prevalence leads to a positively valued $\langle v'w' \rangle^+$ on the top side of the elliptical pipe (see Fig. 11(d)). A comparison of Figs. 21(a)–21(c) reveals that, as the rotation number increases, the probability of Q1, Q2 (ejection), and Q3 events falls monotonically, while that of Q4 (sweep) events increases monotonically. The reduction in the probability of Q1 and Q2 events, in particular, is a result of the Coriolis force in the y direction ($2\Omega w$) emerging from the imposed system rotation, which works to oppose fluid motions from the top wall down to the core turbulent region in the pipe center. Since the initial formation of hairpin structures requires strong initial ejection events [31,32], this trend in the JPDF of w' and $-v'$ with an increasing rotation number plays an important role in the reduction

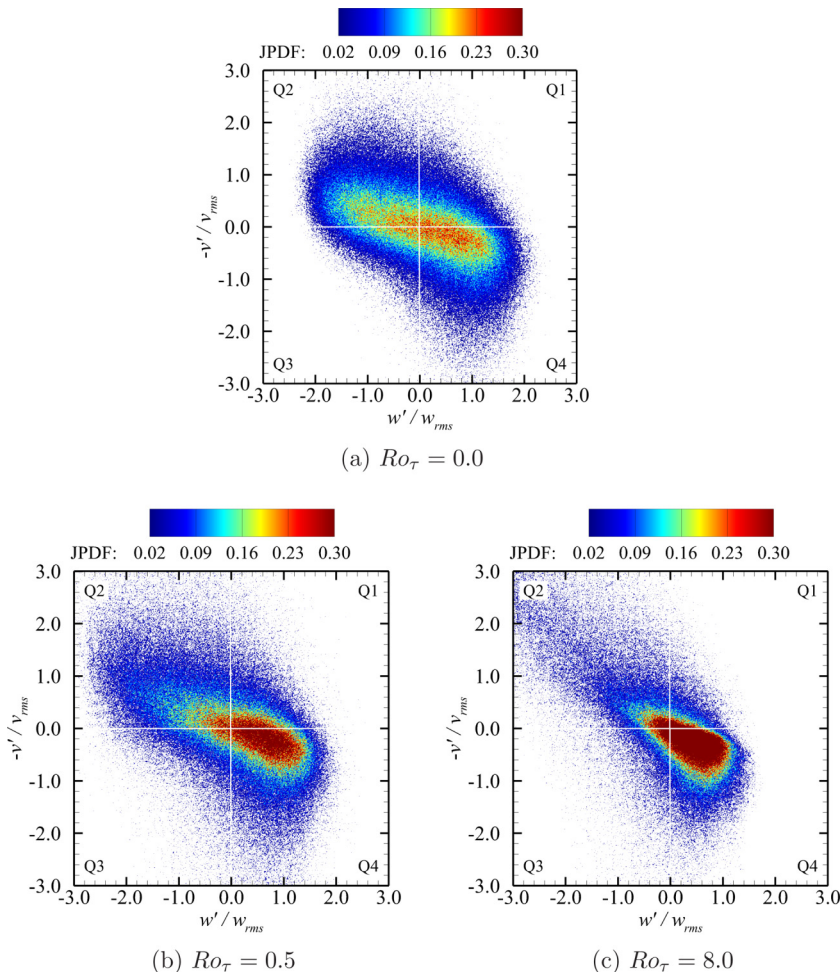


FIG. 21. The JPDF of w' and $-v'$ at $y^+ = 14.1$ measured from the pressure wall along the minor axis for different rotation numbers. The four quadrants are divided by thin white lines.

of hairpin structures on the pressure side of the pipe observed previously in Fig. 19(c). A further examination of Figs. 21(a)–21(c) reveals that, while the probability of ejection and sweep events reduces and increases, respectively, as the rotation number increases from $Ro_\tau = 0$ to $Ro_\tau = 8.0$, strong ejection events (with large magnitudes of $-v'$ and w') become more likely than strong sweep events, as indicated by the long tail observed in the second quadrant (Q2) of Fig. 21(c). This explains the behavior of near-wall streaks observed in Fig. 20(c), which features a relatively greater number of weak high-momentum streaks accompanied by a much smaller number of strong low-momentum streaks.

IV. CONCLUSIONS

The effects of spanwise system rotation on the turbulent flow in an elliptical pipe have been studied using DNS at eight rotation numbers varying from $Ro_\tau = 0.0$ to 24.0 . The effects of Coriolis forces on the flow is identified by comparing the rotating flows with the nonrotating flow. To capture the largest turbulent eddy scales in the axial direction, the pipe length is extended to $L_z = 20\pi b$, which is the longest in the current literature of DNS of nonrotating elliptical pipe flows.

In a nonrotating elliptical pipe flow ($Ro_\tau = 0.0$), secondary flows appear in the cross-stream plane, characterized by two pairs of counterrotating mean vortical structures separated by the minor axis, which transport high-momentum fluid from the pipe core to the ends of the major axis, and low-momentum fluid from the ends of the minor axis to the turbulent pipe core. It is observed that these mean flow patterns are highly sensitive to the Coriolis effect and immediately collapse as soon as system rotation is imposed, resulting in a single pair of counterrotating vortices separated by the minor axis, which work to transport low-momentum fluid from the suction side of the elliptical pipe to its pressure side. This leads to a monotonic decrease in the wall friction velocity on the suction side of the pipe and a general reduction of the bulk mean velocity with an increasing rotation number. Furthermore, it is observed that a Taylor-Proudman region appears along the axis of rotation in response to the system rotation imposed, and its extent increases monotonically as the rotation number increases.

For a nonrotating elliptical pipe flow, the profiles of all nontrivial Reynolds normal and shear stress components are symmetrical about the axial center. Once the system rotation is imposed, the symmetry is destroyed by the Coriolis force. A general trend is that the values of all the Reynolds stress components decrease monotonically near the suction side of the elliptical pipe as the rotation number increases. At $Ro_\tau = 24.0$, the values of these Reynolds stress components become trivial, clearly indicating a state of complete laminarization. It is observed that the peak of axial Reynolds normal stress component $\langle w'w' \rangle^+$ on the suction side not only decreases monotonically in magnitude but also drifts toward the pressure side of the pipe as the rotation number increases. In fact, this trend of peak migration with an increasing rotation number is general for all four nontrivial Reynolds stress normal and shear components.

Through a comparative study of the premultiplied spectra of axial, wall-normal, and spanwise velocity fluctuations, it is observed that the magnitude of the axial component $k_z^+ \phi_{33}^+$ is much greater than those of $k_z^+ \phi_{22}^+$ and $k_z^+ \phi_{11}^+$, indicating that the axial velocity fluctuations make the greatest contribution to the TKE of the flow. As the rotation number increases from $Ro_\tau = 0.0$ to 0.25, an initial increase in the peak energy $k_z^+ \phi_{33}^+$ is observed. However, as the rotation number continues to increase from $Ro_\tau = 0.25$ to 24.0, the magnitude of $k_z^+ \phi_{33}^+$ decreases monotonically until it reaches zero for all wavelengths at $Ro_\tau = 24.0$, which is a reflection of the laminarization process. In the nonrotating case, the characteristic wavelength corresponding to the most energetic eddies, as indicated by the mode of $k_z^+ \phi_{33}^+$, is $\lambda_z^+ \approx 1260$. As the rotation number increases to $Ro_\tau = 1.0$, the mode extends to $\lambda_z^+ \approx 2820$, indicating that the Coriolis forces facilitate a significant initial growth in the axial characteristic length scale of the most energetic eddies.

In the nonrotating flow case, the budget balance of Reynolds stresses is dominated by the production term for $\langle w'w' \rangle^+$ and $\langle v'w' \rangle^+$ and by the pressure-strain term for $\langle v'v' \rangle^+$. In response to the system rotation imposed, the Coriolis term appears, which works to transport energy between $\langle w'w' \rangle^+$ and $\langle v'v' \rangle^+$ depending on the sign of $\langle v'w' \rangle^+$ (because $C_{22}^+ \equiv -C_{33}^+ \equiv 4\Omega \langle v'w' \rangle^+$), and also transports the differential energy (between two normal components) into the shear component $\langle v'w' \rangle^+$ at a rate of $-2\Omega(\langle v'v' \rangle^+ - \langle w'w' \rangle^+)$. At a relatively high rotation number of $Ro_\tau = 8.0$, the Coriolis term C_{23}^+ acts as an additional source of energy in the near-wall region of the pressure side, and the diffusion term D_{23}^+ becomes an important energy sink counteracting the role of C_{23}^+ . Also at $Ro_\tau = 8.0$, the Coriolis term C_{22}^+ becomes dominant source of energy in the near wall region of the pressure side, counterbalanced by the pressure-strain term Π_{22}^+ in the budget balance of $\langle v'v' \rangle^+$.

The effects of system rotation on coherent structures have been studied by comparing three cases of different rotation numbers. In the nonrotating case, hairpin structures are symmetrically distributed on the top and bottom sides of the elliptical pipe, but markedly reduced on the left and right sides of the pipe, suggesting that an increased degree of curvature close to the two ends of the major axis poses an impediment to the formation of hairpin structures. As the rotation number increases from $Ro_\tau = 0.0$ to 0.5, hairpin structures become less populated and significantly shorter in the axial direction in response to the secondary flow induced by the Coriolis force. As the rotation number further increases to $Ro_\tau = 8.0$, the strength of the secondary flow is significantly enhanced, which pushes the coherent structures toward the pressure side of the pipe, inhibiting the normal

bursting behavior of the flow, a mechanism that is essential for the formation and evolution of hairpin structures. As such, the formation of hairpin structures is greatly impeded on the pressure side and laminarization spreads throughout the suction side of the pipe.

It is observed that the axial length scale of the near-wall streaky structures reduces significantly as the rotation number increases. A quadrant analysis of the JPDFs of velocity fluctuations reveals that as the rotation number increases, the probability of Q1, Q2 (ejection), and Q3 events falls monotonically, while that of Q4 (sweep) events increases monotonically. The reduction in the probability of Q1 and Q2 events, in particular, is a result of the vertical component of the Coriolis force ($2\Omega w$), which works to oppose fluid motions from the top wall down to the core turbulent region. Furthermore, as the rotation number increases from $Ro_\tau = 0.0$ to 8.0, strong ejection events become more probable than strong sweep events, which results in a relatively greater number of weak high-momentum streaks and a relatively smaller number of strong low-momentum streaks in near-wall regions.

Finally, it should be indicated that this research is motivated based on the observation that the number of DNS studies of stationary (nonrotating) elliptical pipe flows is rather limited, and there is lacking of a study of rotating elliptical pipe flow in the current literature. As the first DNS study, here we focus on the rotating effects by comparing sixteen test cases of different rotation numbers at a fixed ellipse aspect ratio of $AR = 2 : 1$ and a fixed low nominal Reynolds number of $Re_\tau = 180$. In future studies, besides the rotation number effects, the influences of the aspect ratio and Reynolds number can be also investigated. Furthermore, the budget balance of Reynolds stresses has been examined in the physical space in this research, and the study can be refined by examining also the transport process of Reynolds stresses in the spectral space. Additionally, the effect of system rotation on turbulent heat transfer in an elliptical pipe flow can be explored in future studies.

ACKNOWLEDGMENTS

The parallel computing resources and data storage space required for conducting this research were based on WestGrid (Western Canada Research Grid) supercomputers. The spectral-element code developed by Blackburn and Sherwin [22] was critical for obtaining the data here presented. Their contributions are greatly appreciated.

-
- [1] J. P. Johnston, R. M. Halleen, and D. K. Lezius, Effects of spanwise rotation on the structure of two-dimensional fully developed turbulent channel flow, *J. Fluid Mech.* **56**, 533 (1972).
 - [2] D. J. Tritton, Stabilization and destabilization of turbulent shear flow in a rotating fluid, *J. Fluid Mech.* **241**, 503 (1992).
 - [3] R. Kristoffersen and H. I. Andersson, Direct simulations of low-Reynolds-number turbulent flow in a rotating channel, *J. Fluid Mech.* **256**, 163 (1993).
 - [4] O. Iida, K. Miyamoto, and Y. Nagano, Structure of turbulent channel flow under spanwise system rotation, *J. Fluid Sci. Tech.* **2**, 547 (2007).
 - [5] O. Grundestam, S. Wallin, and A. V. Johansson, Direct numerical simulations of rotating turbulent channel flow, *J. Fluid Mech.* **598**, 177 (2008).
 - [6] S. Wallin, O. Grundestam, and A. V. Johansson, Laminarization mechanisms and extreme-amplitude states in rapidly rotating plane channel flow, *J. Fluid Mech.* **730**, 193 (2013).
 - [7] Z. Xia, Y. Shi, and S. Chen, Direct numerical simulation of turbulent channel flow with spanwise rotation, *J. Fluid Mech.* **788**, 42 (2016).
 - [8] G. Brethouwer, Statistics and structure of spanwise rotating turbulent channel flow at moderate Reynolds numbers, *J. Fluid Mech.* **828**, 424 (2017).
 - [9] M. Oberlack, W. Cabot, B. A. Pettersson Reif, and T. Weller, Group analysis, direct numerical simulation and modelling of a turbulent channel flow with streamwise rotation, *J. Fluid Mech.* **562**, 383 (2006).

- [10] I. Recktenwald, T. Weller, W. Schröder, and M. Oberlack, Comparison of direct numerical simulation and particle-image velocimetry data of turbulent channel flow rotating about the streamwise axis, *Phys. Fluids* **19**, 085114 (2007).
- [11] Z. Yang and B.-C. Wang, Capturing Taylor-Görtler vortices in a streamwise-rotating channel at very high rotation numbers, *J. Fluid Mech.* **838**, 658 (2018).
- [12] H. Wu and N. Kasagi, Effects of arbitrary directional system rotation on turbulent channel flow, *Phys. Fluids* **16**, 979 (2004).
- [13] C. G. Speziale, Numerical study of viscous flow in rotating rectangular ducts, *J. Fluid Mech.* **122**, 251 (1982).
- [14] J. Pallares and L. Davidson, Large-eddy simulations of turbulent flow in a rotating square duct, *Phys. Fluids* **12**, 2878 (2000).
- [15] Y.-J. Dai, W.-X. Huang, C.-X. Xu, and G.-X. Cui, Direct numerical simulation of turbulent flow in a rotating square duct, *Phys. Fluids* **27**, 065104 (2015).
- [16] X. Fang, Z. Yang, B.-C. Wang, and D. J. Bergstrom, Direct numerical simulation of turbulent flow in a spanwise rotating square duct at high rotation numbers, *Int. J. Heat Fluid Flow* **63**, 88 (2017).
- [17] Z.-P. Zhang and B.-C. Wang, Direct numerical simulation of turbulent flow in a circular pipe subjected to radial system rotation, *Flow, Turbul. Combust.* **103**, 1057 (2019).
- [18] D. Cain and J. Duffy, An experimental investigation of turbulent flow in elliptical ducts, *Int. J. Mech. Sci.* **13**, 451 (1971).
- [19] N. Nikitin and A. Yakhot, Direct numerical simulation of turbulent flow in elliptical ducts, *J. Fluid Mech.* **532**, 141 (2005).
- [20] T. V. Voronova and N. V. Nikitin, Direct numerical simulation of the turbulent flow in an elliptical pipe, *Comput. Math. Math. Phys.* **46**, 1378 (2006).
- [21] T. V. Voronova and N. V. Nikitin, Results of direct numerical simulation of turbulent flow in a pipe of elliptical cross-section, *Fluid Dyn.* **42**, 201 (2007).
- [22] H. M. Blackburn and S. J. Sherwin, Formulation of a Galerkin spectral element-Fourier method for three-dimensional incompressible flows in cylindrical geometries, *J. Comput. Phys.* **197**, 759 (2004).
- [23] G. Karniadakis and S. Sherwin, *Spectral/hp Element Methods for Computational Fluid Dynamics* (Oxford University Press, New York, 2005).
- [24] M. Di Liberto, I. Di Piazza, and M. Ciofalo, Turbulence structure and budgets in curved pipes, *Comput. Fluids* **88**, 452 (2013).
- [25] A. Bolis, C. Cantwell, D. Moxey, D. Serson, and S. J. Sherwin, An adaptable parallel algorithm for the direct numerical simulation of incompressible turbulent flows using a Fourier spectral/hp element method and MPI virtual topologies, *Comput. Phys. Commun.* **206**, 17 (2016).
- [26] S. B. Pope, *Turbulent Flows* (Cambridge University Press, Cambridge, UK, 2000).
- [27] J. G. M. Eggels, F. Unger, M. H. Weiss, J. Westerweel, R. J. Adrian, R. Friedrich, and F. T. M. Nieuwstadt, Fully developed turbulent pipe flow: A comparison between direct numerical simulation and experiment, *J. Fluid Mech.* **268**, 175 (1994).
- [28] X. Wu and P. Moin, A direct numerical simulation study on the mean velocity characteristics in turbulent pipe flow, *J. Fluid Mech.* **608**, 81 (2008).
- [29] C. Chin, A. S. H. Ooi, I. Marusic, and H. M. Blackburn, The influence of pipe length on turbulence statistics computed from direct numerical simulation data, *Phys. Fluids* **22**, 115107 (2010).
- [30] J. Kim, P. Moin, and R. Moser, Turbulence statistics in fully developed channel flow at low Reynolds number, *J. Fluid Mech.* **177**, 133 (1987).
- [31] J. Zhou, R. J. Adrian, S. Balachandar, and T. M. Kendall, Mechanisms for generating coherent packets of hairpin vortices in channel flow, *J. Fluid Mech.* **387**, 353 (1999).
- [32] R. J. Adrian, Hairpin vortex organization in wall turbulence, *Phys. Fluids* **19**, 041301 (2007).